Time Resolved Spectroscopy of Carriers Dynamics in Superlattices and Quantum Wells

Thesis for the Ph.D. Degree

by

Guy Cohen

Braun Center for Sub-micron Research
Department of Condensed Matter Physics

Submitted to the Scientific Council

of the Weizmann Institute of Science

July 1995

This work was carried out under the supervision of Prof. I. Bar-Joseph in the Department of Condensed Matter Physics, at the Weizmann Institute of Science, Rehovot, Israel.

Acknowledgments

I wish to thank those who helped me with this work. First to my supervisor Prof. Israel Bar-Joseph for his guidance encouragement and help. The wide scope of his advice, concerning professional subjects as well as others, is highly appreciated. Thanks are due to the students in the optical laboratory: Shimshon Bar-ad, Gleb Finkelstein and Guy Eytan, that were a great resource for the exchange of ideas and techniques. Thanks to Hadas Shtrikman and Vladimir Umansky for growing the MBE samples. I wish to acknowledge the help of Michael Rappaport on the early stages of my work. Thanks are due to Prof. S. Gurvitz and B. Deveaud for their cooperation in the research on the couple quantum wells system. Last but not least - thanks to all the students, technicians, secretaries and staff members of the Braun Center for Sub-micron Research for making this center a friendly place to work.

Abstract

In this thesis we investigate carriers dynamics in GaAs/AlGaAs superlattices subjected to external fields that directly affect the inter-well tunneling: electric fields normal to the superlattice layers and magnetic fields parallel to them. We apply time resolved optical techniques, such as differential absorption and four wave mixing, together with conventional continuous wave techniques, such as transmission and photo-current spectroscopy.

Starting with the investigation of the coupling between tunneling and relaxation, we study the decay of electrons from a symmetric coupled quantum wells system to a continuum of states via a potential barrier. We demonstrate that at the limit of a thin barrier the decay rate *decreases* with decreasing barrier thickness and the splitting of the electron energy levels disappears. Next we study the electron transport in superlattices subjected to normal electric fields with an emphasize on the Stark ladder regime. We find that the electron motion across the superlattice is governed by a competition between two processes: the destruction of the mini-band and tunneling into a higher mini-band. When a Stark ladder is optically observed, the mobility of electrons in a direction normal to the layers is *reduced*, as we gradually increase the applied fields. This marks the electron localization and the destruction of the mini-band by the electric field. At higher fields, when Stark localization is complete, tunneling into higher mini-band dominates and the electron velocity increases with field.

A large part of this work is devoted to the investigation of optical properties of narrow band superlattices. These structures are characterized by a mini-band width of the order of the exciton binding energy. We observe a modified Stark ladder, with both the negative and positive order transitions (inter-well excitons) appearing above the zero order one (intra-well exciton). We find field dependent temporal oscillations in the four wave mixing signal and show that they results from exciton quantum beats. Application of a magnetic field parallel to the layers of this structure reveals a phenomenon that its observation was eluded in superlattices so far: Fano interference between an exciton level located in one well and a continuum of states located in an adjacent one. We demonstrate how by varying the strength of the magnetic field we are able to tune the energy of a spatially indirect exciton resonance relative to a continuum edge, hence vary the coupling between the two. We measure the transmission spectra and the four wave mixing decay

patterns and show that both are substantially modified as the exciton crosses the continuum edge.

Contents

Contents 1

Symbols and Abbreviations 2

1. Introduction 5

    1.1 Superlattices 5

    1.2 Superlattices in the presence of a constant electric field 7

    1.3 Superlattices in the presence of a constant magnetic field 10

    1.4 Optical excitation in quantum wells and superlattices 12

2. Research objectives 14

3. The experimental methods 16

    3.1 Time resolved optical methods 16

        3.1.1 Differential absorption 16

        3.1.2 Four wave mixing. 17

        3.1.3 Time resolved photo-luminescence 17

    3.2 Continuous wave optical methods 18

        3.2.1 Transmission spectroscopy 18

        3.2.2 Photo-current spectroscopy 18

    3.3 Temporal and spectral resolutions 18

    3.4 The experimental set-up 19

    3.5 Samples growth and processing 20

4. Electron decay from coupled quantum wells to a continuum 22

4.1 The coupled quantum wells system 22

4.2 Theoretical analysis of CQWs 24

4.3 Experimental considerations - a controlled relaxation channel 25

4.4 Experimental results 26

4.5 Discussion - the role of 29

5. Electron transport in the Stark ladder regime 32

5.1 Electron transport in a biased superlattice 32

5.2 The DA signal: origin and temporal evolution 33

5.3 Experiments 34

5.3.1 Stark ladder formation 34

5.3.2 Time resolved measurements 36

5.4 The electrons traversal times - quantitative models 38

5.5 Summary and Discussion 40

6. The excitonic interaction 41

6.1 Continuous wave measurements 41

6.1.1 A modified Stark ladder 41

6.1.2 A local tight binding model for the narrow band superlattice. 44

6.2 Time resolved measurements 46

6.2.1 Four wave mixing 46

6.2.2 Exciton quantum beats 47

6.3 Summary and discussion 49

7. Fano interference in a parallel magnetic field 50

7.1 Introductory review 51

7.1.1 Exciton in a superlattice subjected to a parallel magnetic field. 51

7.1.2 Fano interference 52

7.2 Experiments 53

7.2.1 Transmission spectroscopy 53

7.2.2 FWM experiment 55

7.3 Interpretation 56

7.3.1 Fano interaction between a two dimensional continuum and an exciton 56

7.3.2 Comparison with experiments 57

7.4 summary 58

8. Summary 60

9. References 61

Publications Related to This Work 65

Appendix A 66

Symbols and Abbreviations

1D - One dimensional

2D - Two dimensional.

3D - Three dimensional.

$A(r)$ - Vector potential.

B - Magnetic field.

c - Speed of light.

C - Capacitance per unit area.

CQWs- Coupled quantum wells.

d - Superlattice period.

D - Diffusion coefficient.

$\mathcal{D}$ - Excitation operator.

DA - Differential absorption.

e - Electron charge.

eV - Electron Volt.

E_n - Energy of the n-th level of a quantum well.

E_{exc} - Indirect exciton energy.

$E_b^{(\nu)}$ - Exciton binding energy with an electron and a hole wave functions centered ν periods away from each other.

$f(E)$- Energy shift due to Fano interference.

F - Electric field.

fs - Femtosecond.

FWM- Four wave mixing.

h, $\hbar$ - Planck's constant.

H - Hamiltonian.

$J_i(x)$ - Bessel function of order i .

k, $k_\perp$,$k_{||}$- Electron momentum: total, normal, and parallel to layers, respectively.

K - Kelvin.

m^* - Effective mass.

m_0 - Electron rest mass.

meV - Mili-electron Volt.

p - Momentum operator.

P - Principal value of an integral.

ps - Picosecond.

PL - Photo-luminescence.

R - Resistance per square.

R_y - Rydberg energy.

S, S_0 - Area of sample and cross section of impinging beam, respectively.

t - time.

$\tilde{T}$ - First moment of the decay rate.

T_2 - Phase relaxation rate.

$u(r)$ - Periodic part of a Bloch function at the center of the Brillouin zone.

v - Tunneling operator.

V - Volt.

$\tilde{V}$ - Matrix element for tunneling.

$V(r)$ - Potential energy.

$V_s(t)$ - Local screening potential.

V_E - Energy dependent coupling term between a discrete state and a continuum state.

W - Watt.

z_0 - Guiding center position of electron in a magnetic field.

α - Absorption coefficient.

Γ_0 - Decay rate.

δ - Energy splitting between two degenerate energy levels.

Δ - Mini-band width.

Δ_0 - Level shift.

$\tilde{\Delta}$ - Energy mismatch between two levels.

ε_n - Energy level in a system composed of several wells.

$\mathcal{E}_i$ - Optical field amplitude.

$(\nu)_{HH/LH}$ - Stark ladder state of index ν, The subscript stands for excitation from the heavy hole and light hole respectively

λ - Polarization vector.

Λ - Modulus of a transfer integral between adjacent wells.

Ω - Energy difference between indirect exciton and direct continuum edge.

ρ_0 - Maximal value for a density of states in a single mini-band superlattice.

$\rho(\varepsilon)$ - Energy dependent density of states.

τ_B - Period of Bloch oscillation.

τ_c - Voltage diffusion characteristic time.

τ_d - Time delay between light pulses.

τ_{scat} - Scattering time.

τ_{tun} - Tunneling time.

τ_{tr} - Traversal time across a superlattice.

ω - Oscillation frequency of a FWM signal.

ω_c - Cyclotron energy.

ξ - Localization length.

1. Introduction

1.1 Superlattices

Superlattices are periodic structures composed of alternating layers of low and high gap materials. The high gap materials create potential barriers that confine the electrons motion to be within the planes of the low gap material layers. This confinement results in a modulation of the potential along the direction normal to the layers, where each layer of a low gap material constitute a potential well. These structures are referred to as superlattices if the separating barriers are made low and narrow enough to enable tunneling between adjacent wells. The quantum coupling then results in a formation of mini-bands and mini-gaps in the energy spectrum.[1]

Superlattices are, therefore, a generalized realization of the periodic Kronig Penney potential.[2] Their appeal stems from their physical measures.[3] While conventional crystals have band widths in the range of a few electron Volts and a lattice period of a few angstroms, in superlattices the corresponding parameters can be tailored to be a few tens of mili-electron Volts and a few nanometers. Moderate electric fields of 10^4 - 10^5 V/cm are then strong enough to produce a potential drop per period of the order of a mini-band width in typical superlattices. In bulk materials the corresponding value is larger than 10^7 V/cm. This field corresponds to a potential drop of ~0.3 Volts over typical inter-atomic distances of 3 Å, and can modify the atomic bonds. Similar considerations hold for the application of magnetic fields. For example, a 10 Tesla field corresponds to magnetic length of 80 Å. While in bulk material this length covers many unit cells, in superlattices it can cover one period or even less .

A tight binding analysis of a superlattice composed of $2N+1$ wells leads to a quasi continuous dispersion relation for its mini-band[4]

$$\varepsilon_q = E_1 - 2\Lambda\cos(qd) \qquad \text{with} \quad qd = i\pi/2(N+1) \qquad 1 \le i \le 2N+1 \tag{1.1}$$

and the corresponding eigenfunctions are

$$\chi_q(z) = \sum_{n=-N}^{N} C_{nq}\varphi(z-nd) \tag{1.2}$$

with

$$C_{nq} = 1/(N+1)^{1/2} \begin{cases} \cos(nqd) & qd = j\pi/(N+1) \quad (1 \le j \le N) \\ \sin(nqd) & qd = \left(j' + \frac{1}{2}\right)\pi/(N+1) \quad (0 \le j' \le N) \end{cases} \tag{1.3}$$

where E_1 is the isolated well energy level, Λ is the modulus of the transfer integral between adjacent wells, d is the superlattice period, and $\varphi(z)$ is the wave-function of an isolated well. The corresponding density of states is:

$$\rho(\varepsilon) = \begin{cases} 0 & \varepsilon < E_1 - 2\Lambda \\ \frac{\rho_0}{\pi} \arccos\left(\frac{-\varepsilon + E_1}{2\Lambda}\right) & |\varepsilon - E_1| < 2\Lambda \\ \rho_0 & \varepsilon > E_1 + 2\Lambda \end{cases} \tag{1.4}$$

where

$$\rho_0 = \frac{m^*(2N+1)S}{\pi\hbar^2} \quad . \tag{1.5}$$

S is the area of the sample and m^* is the effective mass. The probability amplitude of four wave functions having the lowest energies and a superlattice density of states are

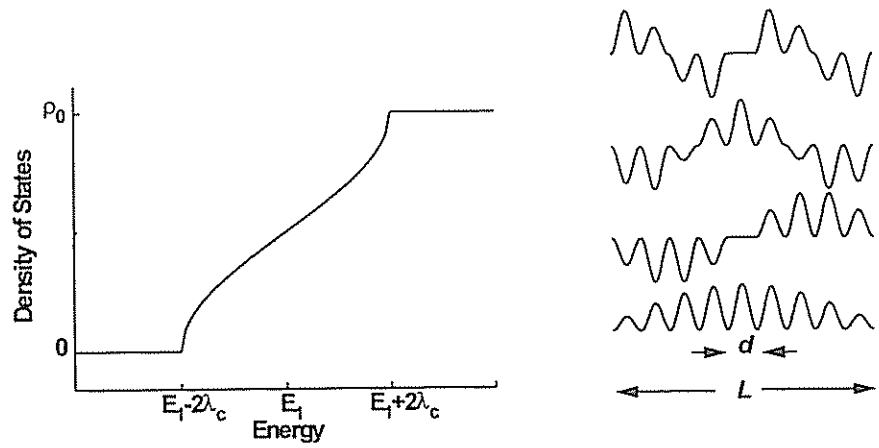

(a) (b)

Fig. 1.1: (a) A superlattice density of states (Eq. 1.4). (b) The probability amplitude of four wave functions having the lowest energy, in a 9 wells superlattice at a flat band condition (Eqs. 1.2 and 1.3). d and L are the superlattice period and length, respectively.

shown in Fig. 1.1.

It should be noticed that the potential modulation and carriers confinement occur only in the growth direction. Carriers having energies within the mini-gap range are free to move in the plane of the superlattice wells. Thus, the term quasi mini-gap is often used in the literature to describe the superlattice gap.

In this work we are concerned with superlattices composed of GaAs and AlGaAs as the low and high gap materials, respectively. All the results derived so far can be directly applied to the conduction band electrons. A few modifications are needed when the valence band is considered. These are traced back to the properties of the bulk GaAs valence band. The upper edge of this band consists of two sub-bands, the heavy and light hole, which are degenerate at $k = 0$. In quantum wells this degeneracy is lifted.[1] Close enough to the center of the Brillouin zone the heavy hole band edge becomes the upper one and the light hole band lies below. The effective masses of the heavy hole and the electron at the band edges in GaAs is $0.62m_0$, and $0.067m_0$, respectively, where m_0 is the free electron mass.[5] Consequently, the mini-band width of the heavy hole is much narrower than that of the electron. This mini-band is, therefore, more sensitive to external perturbations and is destroyed much faster than the electron mini-band at similar conditions (e.g. applied external fields). In practice the heavy hole mini-band width can be smaller than the energy fluctuations due to differences in the widths of the superlattice wells. The translational symmetry is then broken and the holes are localized already at a flat band condition.

1.2 Superlattices in the presence of a constant electric field

In the presence of a constant electric field, F, applied normal to the layers, the continuous mini-band spectrum is replaced by discrete, evenly spaced, energy levels known as the Wannier-Stark ladder:[4]

$$\varepsilon_\nu = E_1 + \nu eFd \qquad -N \le \nu \le +N \tag{1.6}$$

The corresponding eigenfunctions, $\chi_\nu(z)$, are given by Eq. 1.2 with

$$C_{n\nu} = J_{n-\nu}(2\Lambda / eFd) \tag{1.7}$$

where $J_i(x)$ is a Bessel function of order i. The properties of the Bessel functions imply that increasing F will cause the ν-th wave function, $\chi_\nu(z)$, to be concentrated in the vicinity of the ν-th well. Energy levels of a superlattice in the presence of an electric field and the corresponding probability density are plotted in Fig. 1.2.

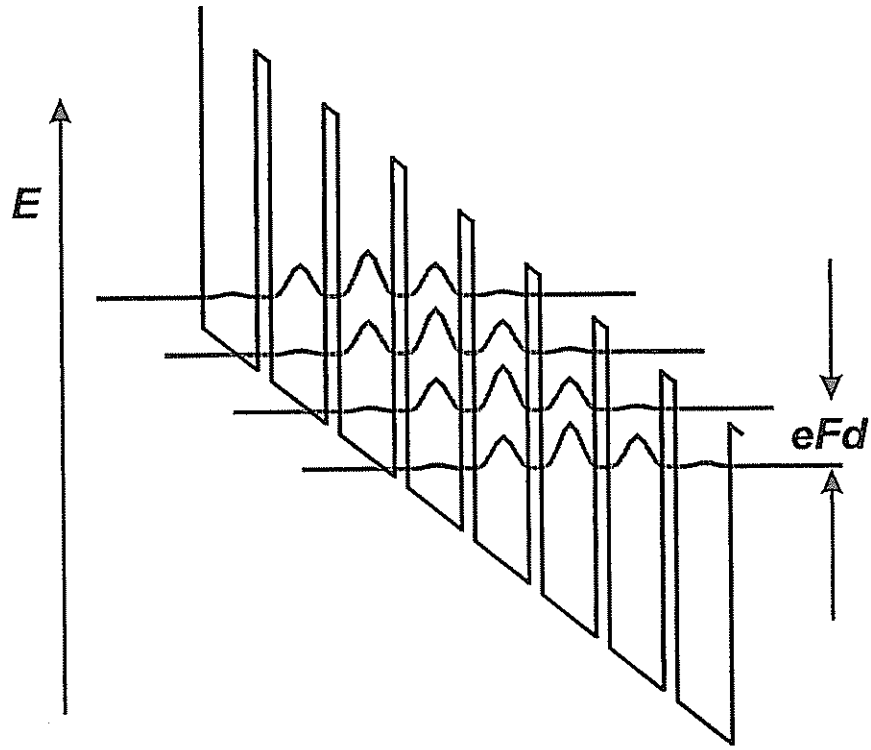

Fig. 1.2: Energy levels and the wave functions probability density in a superlattice subjected to an electric field (Eqs. 1.6 and 1.7). Here, $eFd = 0.38\Delta$, where Δ is the mini-band width.

The temporal manifestation of the Wannier Stark ladder is the oscillatory motion of electrons in a periodic potential named after Bloch.[6] A Bloch electron subjected to a constant electric field, F, obeys the acceleration theorem, $\hbar dk/dt = eF$, stating that the momentum varies linearly with the field. As a result of crystal symmetry, it is Bragg reflected from the edges of the Brillouin zone. The electrons motion is therefore oscillatory,[6] with an oscillation period $\tau_B = h / eFd$ and is extended over a spatial region $\xi = \Delta / eF$, where Δ is the mini-band width. The energy eFd that characterizes the Bloch oscillations is nothing else but the energy difference between two Wannier Stark states centered in adjacent wells (Eq. 1.6).

The notion of Wannier Stark ladder and the corresponding localization process were a matter of controversy for many years.[7-10] However, it is agreed that the results presented above are correct for finite superlattices. The case of infinite superlattices was treated by Krieger and Iafrate representing the electric field as a time dependent vector potential.[11] They obtained selection rules for the optical transitions that are compatible with those predicted by previous theories of Wannier Stark ladder.

Wannier Stark ladder and Bloch oscillations were never observed experimentally in bulk solids. The main obstacles were the short scattering times (~ 200 fs for optical phonons) and the very strong electric fields (>10^7 V/cm) which are required. The large unit cells of the superlattice and the ability to tailor a narrow mini-band provide a better experimental environment for the realization of these phenomena.

Indeed a renewed interest in the problem was triggered by the development of semiconductor superlattices. It was predicted that Bloch oscillations will be manifested in the transport properties of a superlattice as a negative differential conductivity.[12] Negative differential conductivity was also predicted to occur when considering the strong Stark localization regime, where inelastic hoping between different Stark level states is the transport mechanism[13]. These models were studied experimentally in a series of transport measurements.[14-16] The results, however, were not conclusive.[17] A different scattering process that was considered theoretically is tunneling to the next (mini-)band[18]. It was even argued that this effect is strong enough to prevent the observation of the Wannier Stark ladder.[19]

Optical measurements proved to be more successful in investigating this phenomenon. In 1988 it was shown simultaneously by Mendez *et al.*[20] (using photo-current spectroscopy) and by Voisin *et al.*[21] (using reflection spectroscopy) that the peaks appearing in the optical spectra of short period superlattices at low temperatures are consistent with the notion of the Wannier Stark ladder. These experiments, made possible by the growth of high quality superlattices, have set the stage for an intensive study of fundamental as well as practical aspects of this effect. These include, among others, the investigation of the temperature dependence of Wannier Stark ladder[22], the mixing of several sub-bands[23], and the behavior in crossed electric and magnetic fields[24].

Recently, the experimental effort was extended to the investigation of the coherent motion of electrons in the temporal domain.[25-27] Time resolved four wave mixing and tera Hertz electromagnetic wave emission experiments have demonstrated the appearance

of temporal oscillations, which were attributed to Bloch oscillations.[25] The validity of this interpretation is still under discussion.[28]

1.3 Superlattices in the presence of a constant magnetic field

A magnetic field can be applied upon a superlattice either perpendicular or parallel to the layers.[29] In the first case, the field affects only the electron motion in the superlattice plane. In the second configuration, the magnetic field tends to localize the carriers motion in the same plane as that of the confining potential. We consider here the second configuration, that we find more interesting in the context of superlattices. We shall use the terms normal and parallel fields to denote fields that are applied normal or parallel to the layers throughout this work.

The behavior of the system subjected to a parallel magnetic field is different at low and high fields. We define the low field regime as that where the magnetic cyclotron energy, $\hbar\omega_c$, is smaller than the mini-band width. The underlying physics in that regime is similar to that of a bulk solid.[30] Bulk-like Landau levels are formed within the conduction mini-band width. Semi-classically, the electron motion can be described as performing cyclotron orbits, traversing several barriers during its motion.[30] As the magnetic field is increased the higher Landau levels cross the mini-band upper edge and become dispersive.[31] That is to say that the energies of the guiding centers are not degenerate anymore and depend on their spatial location in the well. A guiding center located in the barrier has a different energy than a one that is centered in the well. The strong field limit is reached when the cyclotron energy exceeds the mini-band width. Then, even the lowest lying Landau level develops a dispersion.[32] In the semi-classical analog, the electron trajectory is a circle, and it is scattered elastically from the walls forming skipping, and even more complicated, orbits.

To understand this system quantitatively let us consider the Hamiltonian of a superlattice conduction band electron in a magnetic field:

$$H = \frac{\hbar^2}{2m^*}\left(p - \frac{e}{c}A(r)\right)^2 + V(z) \qquad (1.8)$$

where $V(z)$ is the superlattice potential and $A(r)$ is a vector potential, which for a magnetic field $B\hat{x}$ parallel to the layers is taken to be $Bz\hat{y}$ (Landau gauge). m^* and p are

the electron effective mass and momentum, respectively. Let us examine first the case where $V(z)$ describes a single quantum well. The zero field wave function, Φ, is proportional then to:

$$\Phi(\vec{r}) \approx e^{-ik_x x} e^{-ik_y y} \varphi(z), \tag{1.9}$$

and the first order correction to the zero field energy due to the applied magnetic field is:

$$E^{(1)} = \frac{e^2 B^2}{2m^* c^2}\left(\frac{c\hbar k_y}{eB} - \langle z \rangle\right)^2 + \frac{e^2 B^2}{2m^* c^2}\left(\langle z^2 \rangle - \langle z \rangle^2\right) \tag{1.10}$$

The first term in Eq. 1.10 describes a parabolic dispersion of the electron energy as a function of its guiding center position $z_0 = c\hbar k_y / eB$ (Fig. 1.3(a)). Using a tight binding approach to describe the energy spectrum of an electron in a superlattice, this term gives rise to a family of intersecting parabolas, one for each well. Tunneling mixes these curves and results in their anti crossing, as shown in Fig. 1.3(b). As the coupling between the wells is increased, the states around the intersection points repel each other more and more to create flat bulk like Landau levels. The second term in Eq. 1.10 represents a simple diamagnetic shift common to all states, with no spatial dispersion.

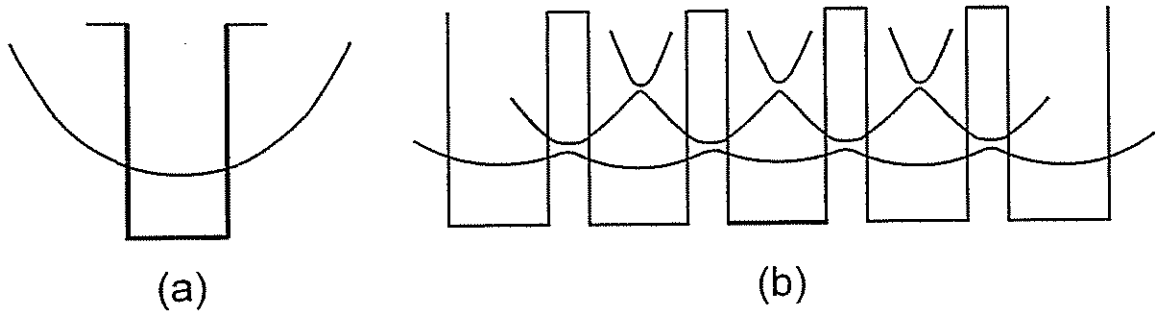

Fig. 1.3: Energy levels in the strong magnetic field limit (Eq. 1.10): (a) in a single well, and (b) in a superlattice.

Optical measurements of a superlattice subjected to a magnetic field in this configuration were made using continuous wave spectroscopy. The measured spectra provided information on the mini-band width, the carriers effective mass, and the characteristic scattering times.[29]

1.4 Optical excitation in quantum wells and superlattices

A large portion of the research on superlattices is made by employing optical techniques. Continuous wave techniques, such as photo-luminescence excitation, and photo-current spectroscopy are widely used in the investigation and characterization of superlattices. In recent years there is a growing use of time resolved optical techniques in studying these structures.

The matrix element for the absorption of light exciting an electron from the heavy hole valence band to the conduction band is[1]

$$\langle f|\lambda \cdot p|i\rangle \approx \lambda \cdot \langle u_f|p|u_i\rangle \int \psi_f^* \psi_i \, d^3r \tag{1.11}$$

where λ is the polarization vector, p is the electron momentum operator, $u(r)$ is the periodic part of the Bloch functions at the center of the Brillouin zone, and

$$\psi(r) = \theta(r_{||})\chi(z). \tag{1.12}$$

here $\theta(r_{||})$ is the wave function in the plane of the layers and $\chi(z)$ is the envelope function in the growth direction. The absorption of light, therefore, is strongly affected by the electron hole overlap integral $\langle \chi_e(z)|\chi_h(z)\rangle$. In many of the cases under consideration it is appropriate to assume that the heavy hole is completely localized and its energy is discrete. The inter-band absorption properties of a superlattice are then a measure of the conduction band eigenfunctions and eigenenergies.

In Fig. 1.4 the energy levels, wave functions and allowed transitions between the heavy hole sub-band and the conduction band of a biased superlattice are plotted. Here and throughout this thesis Stark ladder states are denoted by $(\pm\nu)_{HH}$ and $(\pm\nu)_{LH}$ for excitations from the heavy and light hole sub-bands, respectively. $\pm\nu$ is the index of the electron Stark level energy (Eq. 1.6) counted from the location of the photo excited hole.

In reality, the absorption spectrum of a biased superlattice is dominated by excitons, each of which is related to a different Stark ladder state (see for example Fig. 5.2).[1] We denote these excitons by their electron Wannier Stark state.

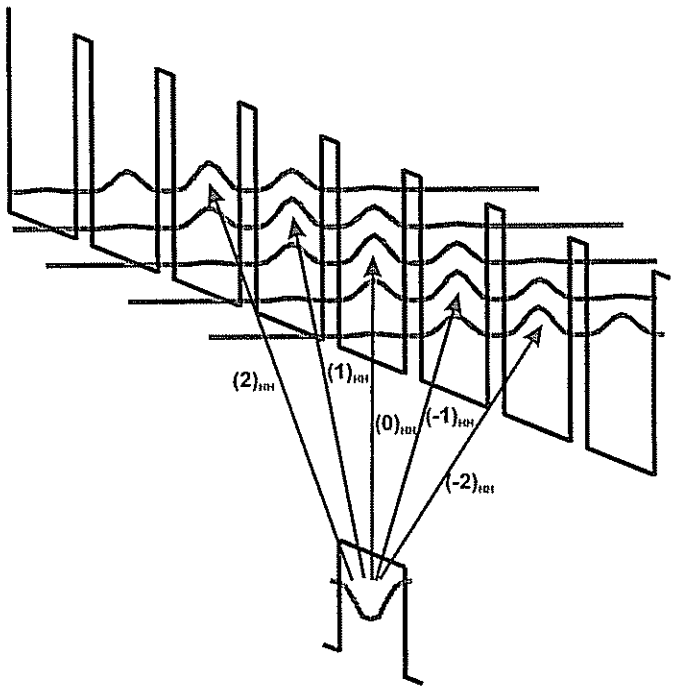

Fig. 1.4: Valence to conduction band optical excitations from a localized heavy hole into different Stark ladder states. The excitations are denoted by the corresponding electron state.

2. Research objectives

In this work we investigate the electron motion in superlattices subjected to external fields. We consider electric and magnetic fields which affect the electron tunneling in the superlattice, namely - an electric field normal to the layers and a magnetic field parallel to them. The tool we use is optical spectroscopy, with a special emphasis on time resolved measurements.

The theory of electrons dynamics in a superlattice subjected to normal electric fields was intensively investigated during the last two decades. However, at the onset of our work the published data was gathered mainly through indirect transport measurements. Our objective was to apply fast optical techniques to study electron transport in these conditions.

Optical spectroscopy allows direct measurements of the electron energy spectrum and dynamics without having to take into account the leads and the effect of current flow. The extreme time resolution available by present day lasers enables performing direct measurements of energy relaxation and scattering processes. Furthermore, minute energy splitting which are hidden by inhomogeneous broadening can be extracted accurately from the beating period they induce in the coherent optical signal. Finally, optical spectroscopy provides us with energy selectivity, which enables us to control precisely the states we excite or probe.

The work is organized as follows:

In chapter 3 we introduce the experimental techniques. These include differential absorption, four wave mixing and photo-luminescence as methods for performing time resolved measurements. Continuous wave photo-current and transmission spectroscopy were used to obtain the complementary spectral information. We then briefly describe the experimental set-up and sample preparation.

In chapter 4 we discuss the interplay between tunneling and a relaxation process in a coupled quantum well system. Relying on the similarity between a coupling to a relaxation channel (e.g. phonon assisted decay) and a coupling to a continuum of states we perform a controlled time resolved experiment on a coupled quantum wells system that one of its wells is coupled to a continuum of states. We show that the electron decay process is affected by quantum interference in an unexpected way: when a coupled

quantum wells system is in contact with a relaxation channel, the electron decay rate through this channel can be slowed down with increasing relaxation rate.

In chapter 5 we describe time of flight measurements of electrons motion across a superlattice subjected to external electric field. We correlate the measured electrons velocity and the observed spectrum at different applied fields. We show that this velocity is non monotonic in the applied field and it becomes slower with increasing field when a Stark ladder is optically observed. We attribute this negative differential velocity to the destruction of the mini-band and to a formation of Stark localized states.

In chapter 6 we focus on the role of excitonic effects in superlattices. To enhance these effects we design a narrow band superlattice in which the coupling between adjacent wells is smaller than the excitonic Rydberg. In this system we find a unique evolution of the Stark ladder spectrum where both the positive and negative index transitions, $(\pm\nu)_{HH}$, are above the zero index transition at low applied electric fields. In the time domain we show field dependent oscillations in the four wave mixing signal and identify them as excitonic quantum beats.

In chapter 7 we study the energy spectrum and dynamics of excitons in a narrow band superlattice subjected to a parallel magnetic field. We show that these can be understood by considering Fano interference between discrete excitonic states and continuum of states in other wells. By changing the magnetic field we tune the energy of the exciton state relative the continuum edge. This system provides a unique opportunity to study Fano interference near this edge. We show that exciton dynamics and the observed spectrum are substantially changed when the discrete level is crossing the continuum edge.

3. The experimental methods

We have used various optical spectroscopic methods to investigate the energy spectrum and the dynamics of electrons in superlattices. One can distinguish between two main groups of techniques: those which are based on very short pulse lasers and those which use continuous-wave lasers. In the following we shall describe the main methods used in our work.

3.1 Time resolved optical methods

3.1.1 Differential absorption

In the differential absorption (DA) technique two beams derived from the same laser are impinging on a sample, at a small angle between them. These beams consist of a train of light pulses that are synchronized, so that each pulse in one beam (termed the probe) is delayed with respect to its matching pulse in the other (termed the pump) by the same amount of time, τ_d (see Fig. 3.1). The pump is modulated by a low frequency chopper (at a few hundreds Hz) and the resulting intensity modulation of the probe after passing through the sample is time integrated by a slow detector using conventional lock-in techniques. The signal is measured as a function of the delay time, τ_d, between the pulses.

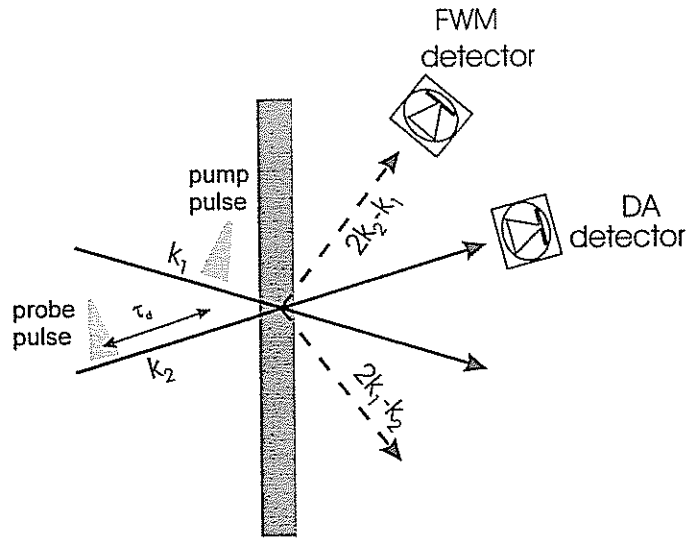

Fig. 3.1: A schematic description of DA and FWM experiments.

The measured quantity is the change in the absorption due to the presence of the pump. Various mechanisms can generate this absorption change. A commonly considered mechanism is phase space filling by the photo-excited electron-hole pairs that causes bleaching of the absorption. The decay of the signal is then a measure of the population relaxation rate. Other processes, such as band gap renormalization and space charge build-up can cause a shift or a broadening of the absorption line. The temporal dependence of the DA signal in those cases can be complicated and will be discussed in the context of specific experiments.

3.1.2 Four wave mixing.

The four wave mixing (FWM) set-up is similar to that of the DA measurement. Here, the integrated intensity of the emitted signal following the coherent excitation by the two beams is detected at a direction $2k_2 - k_1$ or $2k_1 - k_2$ where k_2 and k_1 are the wave vectors of the impinging beams (Fig. 3.1). Here also, the signal is measured as a function of τ_d, the time delay between the exciting pulses.

The signal that is measured in a FWM experiment results from the third order polarization that is induced by the exciting beams. It is proportional therefore to $\mathcal{E}_1\mathcal{E}_2^{\,2}$ ($2k_2 - k_1$ direction) or $\mathcal{E}_2\mathcal{E}_1^{\,2}$ ($2k_1 - k_2$ direction), where $\mathcal{E}_i$ is the optical field amplitude. Its decay is a measure of the phase relaxation rate of the coherent excitation. The phase relaxation time is commonly denoted by T_2 in the terminology of a two level system. The measured decay rate is $2/T_2$ and $4/T_2$ for homogeneous and inhomogeneous broadening, respectively.[33]

3.1.3 Time resolved photo-luminescence

We have also used time resolved photo-luminescence (PL) measurements, performed in collaboration with the CNET laboratory at Lannion France . In this method the system is excited by a pump pulse at an energy, which is larger than the gap. The resulting luminescence is focused on a non-linear crystal together with the probe beam. The intensity of the sum frequency light (probe + PL) is recorded as a function of the time delay between the pump and the probe. Using this method we measure the recombination rate of the photo-excited electron hole pairs.

3.2 Continuous wave optical methods

3.2.1 Transmission spectroscopy

In the transmission spectroscopy method a single beam, emitted from a tunable laser, is optically modulated and passed through a sample. The normalized intensity of this beam is measured as a function of the excitation energy. Using this method we can map the spectral position of the energy levels in a given sample.

3.2.2 Photo-current spectroscopy

Here again, a single light beam from a tunable laser is modulated by an optical chopper and absorbed in the sample. The measured quantity is the excitation induced photo-current that is differentiated from the dark current by a lock-in technique. This photo-current is measured as a function of the excitation energy and the resulting spectrum is a replica of the absorption spectrum. Using this method we can extract information about the spectral position and the relative absorption strength of the energy levels in the measured sample. This method is convenient and efficient when practiced upon biased superlattices. However, in superlattices close to a flat band condition the process of radiative recombination becomes dominant, and reduces the amount of collected photo-current. A comparison of the photo-current spectrum with the absorption spectrum is then made complicated.

3.3 Temporal and spectral resolutions

We now review some of the considerations regarding time resolved methods and their application to the investigation of electron dynamics in superlattices. As an illustrative example we consider the Bloch oscillation phenomenon. The period of one Bloch oscillation τ_B is equal to $(h/\Delta)\cdot(\xi/d)$, where Δ is the mini-band width and (ξ/d) is the localization length in units of the superlattice period, d (section 1.2). To avoid an efficient emission of optical phonons Δ should be smaller than ~36 meV. Taking as a limiting case $(\xi/d)=2$, the fastest oscillations we can measure have a period τ_B ~0.2 ps. τ_B can be made longer by reducing Δ, the mini-band width. However, we are restricted by the optical dephasing of the states involved. The dephasing time in good quality superlattices is at most 2 ps. The need to see three or more oscillations during this

time, in order to identify them as such, restricts their period to be less than 1 ps. These considerations set a range for the period of Bloch oscillations , which can be observed in a coherent optical experiment, $0.2-1$ ps. They also define the time resolution necessary to observe the oscillations, ~100 fs. Commercially available mode locked solid state lasers are now able to provide this time resolution.

improving the temporal resolution is accompanied by an increase in the spectral band-width of the light pulses emitted by the laser. For example, the Styril 8 dye laser emits pulses having a one picosecond auto-correlation width, and ~2 meV spectral band-width, while the corresponding values for our Ti:Sapphire laser are 100 fs and 25 meV, respectively. It is not always advisable, then, to use the shortest pulses available, and the spectral resolution that is needed for properly interpreting the time resolved data has to be considered as well.

3.4 The experimental set-up

The experimental set-up for the time resolved measurements is plotted in Fig. 3.2. It consists of a high power stabilized laser, (Nd:Yag or Argon) (1) pumping a passively mode locked tunable laser (Dye or Ti:Sapphire) (2). This in turn emits short light pulses at a repetition rate of 76 MHz. The tuning range of the pulsed laser is between 720 and 850 nanometers depending on the laser in use. The pulsed beam is split to a pump and a probe (3). The probe beam is passed through a retro-reflector (4) mounted on a linear stepper motor and the pump is passed through an optical chopper (5). The two beams are then entering an array of optical devices (6) utilized for controlling their relative polarization and the width of their cross-sections. They are focused (7) on

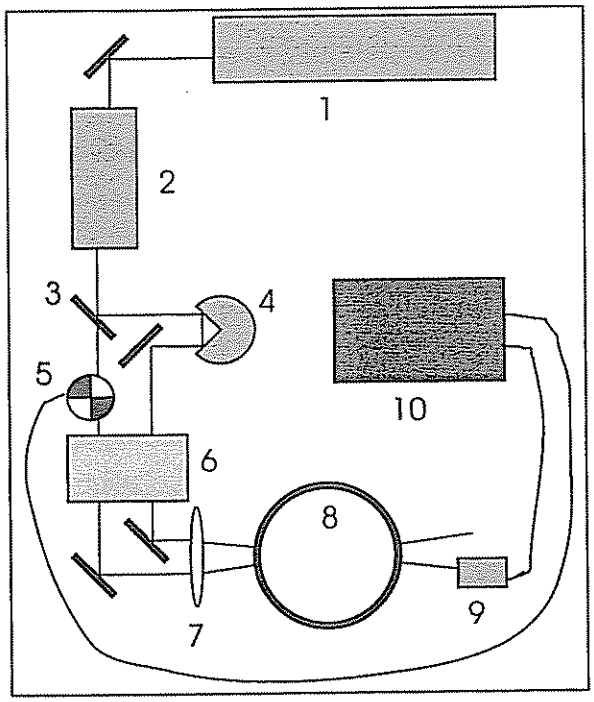

Fig. 3.2: A time resolved experimental set-up. The details are found in the text.

the sample via the optical aperture of a 7 Tesla magneto-optical cryostat (8). A slow detector (9) attached to an electronic analysis unit (10) measures either the intensity of the probe beam (in DA experiments) or the time integrated intensity of the diffracted signal (in FWM experiments). Electronic units are also attached to the sample enable its biasing as well as photo-current measurements. An imaging system (do not appear in the scheme) is used to overlap the two beams on the sample.

3.5 Samples growth and processing

Investigation of biased superlattices requires the ability to apply an external electric field while preventing the flow of currents. This can be done by positioning the investigated superlattice in the intrinsic region of either a p-i-n junction or a Schottky diode (metal-i-n). In some of the optical measurements the sample has to transmit light as well. In this section we describe the process of sample preparation.

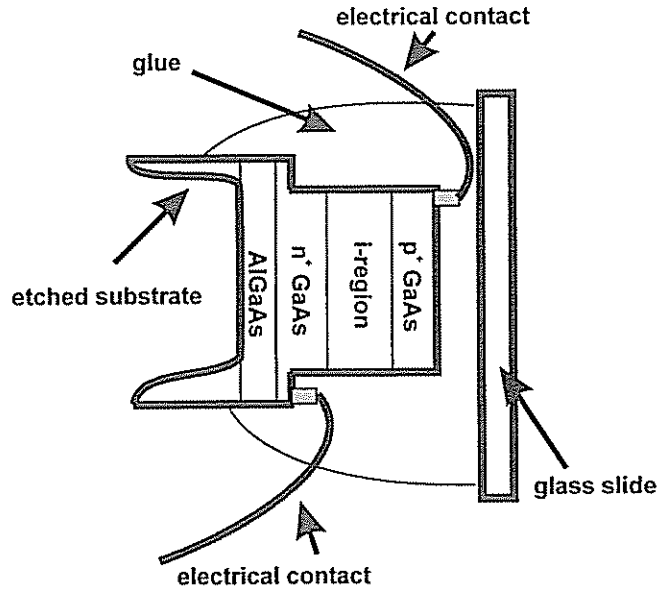

Fig. 3.3: A schematic draw of a single processed diode.

The epitaxial layers are etched to form mesas of $200 \times 200 \mu m^2$ electrically isolated from each other. Electrical contacts are then attached to the top and bottom of each mesa.

In the case of a p-i-n diode the top contact is ohmic and cover only a small part of the mesa, while in Schottky diodes we used a semi-transparent Cr layer, deposited on the whole area of the diode, as the metal gate. The sample is then glued to a thin glass slide and the substrate is removed using a selective wet etch.[34] The contacts are bonded to a ceramic 24 pin header with a via-hole suitable for mounting in the optical cryostat. A schematic view of a fully processed sample is given in Fig. 3.3.

4. Electron decay from coupled quantum wells to a continuum

4.1 The coupled quantum wells system

The electron motion in a superlattice conduction band is dominated by two main processes: coherent tunneling between adjacent wells and incoherent scattering. Our focus in this section is the interplay between these two types of processes. In Fig. 4.1 we sketch a biased superlattice, where tunneling and incoherent scattering processes are marked by arrows. The latter include transitions to a higher energy mini-band, by tunneling or thermionic excitation, and various phonon assisted relaxation channels. One can, however, design a simpler structure, that will capture the essence of the problem, where tunneling is coupled to a single scattering channel. A possible system is the coupled quantum wells (CQWs) that is marked by dashed lines in Fig. 4.1.

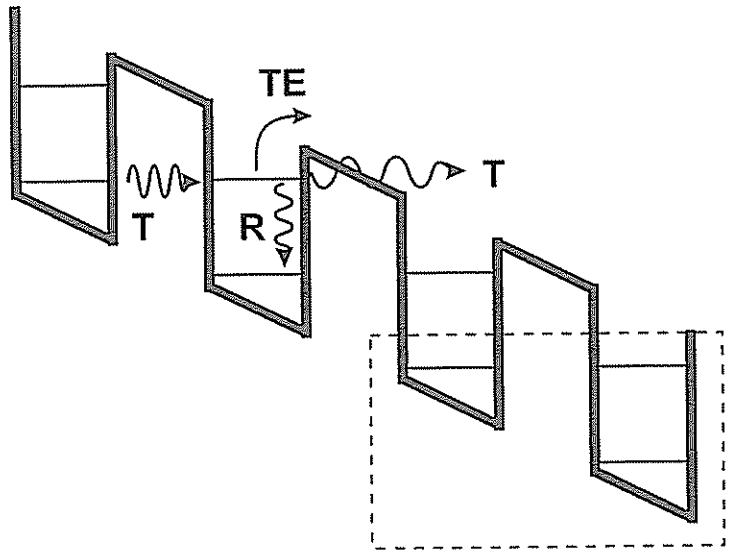

Fig. 4.1: Electron processes in superlattices: (T) tunneling, (TE) thermionic emission, and (R) phonon assisted relaxation.

A CQWs system on which many studies were performed is the *asymmetric* CQWs (Fig. 4.2). It consists of a wide and a narrow well. Alignment of the energy levels, hence the achievement of a resonance condition, is obtained by the application of an external electric field. As the levels are aligned, photo-excited electrons can tunnel resonantly

from the narrow to the wide well, where they relax to the lower energy level by phonon emission. Time resolved PL and DA measurements were used to investigate the dependence of the tunneling times on the level alignment.[35-37] A sharp increase in the electron escape rate from the narrow well was found when a resonance condition was achieved. Coherent motion of an electron wave-packet was also observed in similar systems. Oscillations in the FWM signal and sub millimeter wave emission are the manifestations of this motion.[38,39]

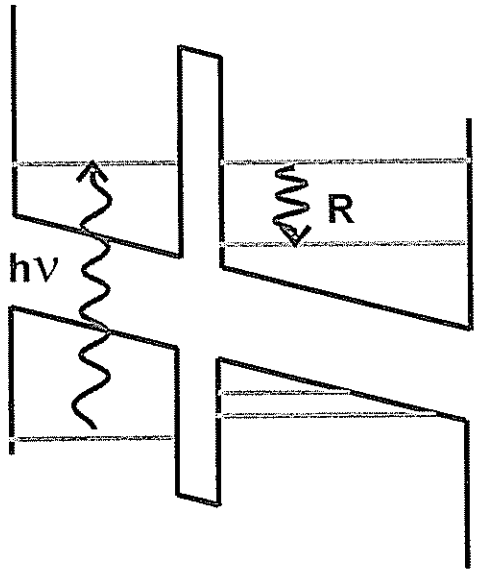

Fig. 4.2: An asymmetric CQWs system at resonance. In resonant tunneling measurements the electron is optically excited in the narrow well ($h\nu$) and relaxes to the lowest lying energy level in the wide well (R).

While all these experiments concentrated on the resonant nature of the tunneling, the effect of electron relaxation on the tunneling process was not studied carefully. A theoretical analysis of the electron decay process in CQWs structures has revealed that it is affected by quantum interference phenomena in an unexpected way.[40] It was shown that when coupled quantum states in CQWs are in contact with a relaxation channel (e.g. decay by phonons to a lower energy level), the electron decay rate through this channel is sometimes *slowed down with increasing relaxation rate*. Similar considerations have led to interpreting the excessively long decay time of holes in CQWs as resulting from inelastic relaxation, which suppress the decay rate.[41] In this chapter we describe a

thorough experimental study of the dependence of the decay rates in CQWs on the strength of a relaxation channel.

4.2 Theoretical analysis of CQWs

Let us start with a theoretical description of a CQWs system that is sketched in Fig 4.2. Following Ref. [40] the electron wave function in the CQWs is given by the solution of an effective Schrodinger equation of the form:

$$i\frac{\mathrm{d}}{\mathrm{d}t}\begin{pmatrix}\varphi_1(t)\\ \varphi_2(t)\end{pmatrix}=\begin{pmatrix}E_1 & \delta/2\\ \delta/2 & E_2+\Delta_0-i\Gamma_0/2\end{pmatrix}\begin{pmatrix}\varphi_1(t)\\ \varphi_2(t)\end{pmatrix} \tag{4.1}$$

where $|\varphi_n(t)|^2$ is the probability to find the system in the n-th well with an energy E_n. Δ_0 and Γ_0 are the level shift and width due to coupling to phonons, respectively, and δ is the energy splitting due to tunneling between the levels of the different wells.

The two eigenvalues of the matrix are:

$$\varepsilon_{1,2}=E_1+\frac{\tilde{\Delta}}{2}-\frac{i\Gamma_0}{4}\pm\frac{1}{2}\sqrt{\tilde{\Delta}^2+\delta^2-(\Gamma_0/2)^2+i\tilde{\Delta}\Gamma_0}\,, \tag{4.2}$$

where $\tilde{\Delta}=\Delta_0+\varepsilon$, $\varepsilon=E_2-E_1$. Let us assume for the moment that $\tilde{\Delta}=0$. We can distinct two regimes: a weak relaxation regime, where $\Gamma_0/2<\delta$, and a strong relaxation one, where $\Gamma_0/2\geq\delta$. It can easily be seen that when $\Gamma_0/2<\delta$ (weak relaxation) we get two *non-degenerate* levels, with an energy splitting which is equal to $\sqrt{\delta^2-(\Gamma_0/2)^2}$. In the opposite case, of $\Gamma_0/2\geq\delta$ (strong relaxation), we get two *degenerate* energy levels and the energy splitting disappears. Thus, the transition from the weak to the strong relaxation regime, is marked by a c*ollapse* in the splitting of the energy levels

Further insight into the behavior of the system is obtained by inspecting the imaginary part of the eigenvalues, which represents the decay time. In the weak relaxation regime we get approximately the same value, $\Gamma_0/2$, for both energy levels. In the strong relaxation regime, however, the imaginary part of the eigenvalues has two different solutions: $\Gamma_0/2$ and $\delta^2/2\Gamma_0$, representing a fast and a slow decay, respectively. Thus, increasing Γ_0 in the weak relaxation regime results in a faster decay of the CQWs system. In the strong relaxation regime, however, the overall time evolution of the system is a two exponential decay. Increasing Γ_0 will cause the fast exponent $(\Gamma_0/2)$ to be even faster, and the slow one $\delta^2/2\Gamma_0$ to be slower. It should be noticed that $\tilde{T}$, the average decay

time, defined as the first moment of the decay rate, $\tilde{T} = -\int_0^\infty t\, \mathrm{d}/\mathrm{d}t[|\varphi_1(t)|^2 + |\varphi_2(t)|^2]\mathrm{d}t$ is equal to:[40]

$$\tilde{T} = \frac{2}{\Gamma_0} + \frac{2\left(\varepsilon^2 + (\Gamma_0/2)^2\right)}{\Gamma_0 \delta} \tag{4.3}$$

and is increasing with increasing Γ_0 in the strong relaxation regime.

Including a finite $\tilde{\Delta}$ would introduce some modifications to that picture, and there will be an energy splitting also in the strong relaxation regime. A quantitative discussion on the role of $\tilde{\Delta}$ is given in section 4.5.

4.3 Experimental considerations - a controlled relaxation channel

It is rather difficult if not impossible to experimentally vary the coupling to phonons, and study the dependence of the decay process on Γ_0, the relaxation rate. An alternative system, which exhibits a similar behavior, is the *symmetric* CQWs, where one of the wells is coupled via a thin barrier to a continuum of states (Fig. 4.3). It was shown in Ref. [40] that the asymmetric CQWs, where the decay is through phonon emission, (Fig. 4.2) and the symmetric CQWs which decays by tunneling (Fig. 4.3) are described by the same effective Schrodinger equation (Eq. 4.1), with Γ_0 being the relaxation rate due to coupling either to phonons or to the continuum states. This similarity is not surprising since the essence of the inelastic scattering process is the high density of final states of the electron phonon system, which makes the process irreversible at low temperatures[42]. The advantage of the symmetric CQWs system in serving as a model for studying the coupling between quantum tunneling and relaxation is obviously the ability to change the relaxation parameters in a controlled

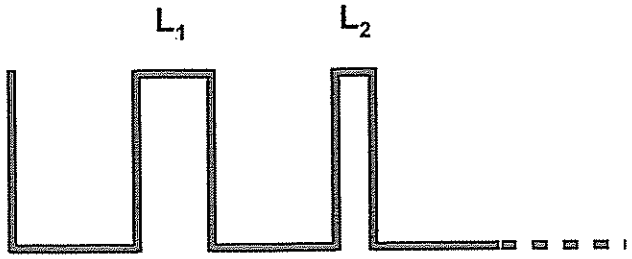

Fig. 4.3: A CQWs system coupled asymmetrically to a continuum of states.

manner. The coupling strength between the two symmetric wells and between the CQWs and the continuum are governed by the widths and heights of the separating potential barriers. These parameters are controlled to a high degree of accuracy during the growth procedure.

To study the dependence of the decay rate on Γ_0, we have grown three different samples with the same structure except for the width of L_2. The exact structure of the three samples we used is found in Appendix. A. The significant part of each sample consists of 10 repetitions of the structure that appears in Fig. 4.3: two 80-Å GaAs quantum wells with a 50-Å $Al_{0.2}Ga_{0.8}As$ barrier between them (designated by L_1), are coupled to a continuum (800-Å wide GaAs layer) through a thin $Al_{0.2}Ga_{0.8}As$ outer barrier of thickness L_2 at one side. The values of L_2 in the three samples are 50, 20, and 10 Å. Hereafter the samples will be labeled by the width of their outer barrier, L_2.

Two complementary experimental techniques were used in this work, time resolved PL and DA. Setting the detection energy to the emission line of the CQWs, the time resolved PL directly measures the recombination rate of electron-hole pairs in the wells. Since the electrons tunneling rate is faster than that of the holes, the decay of the PL signal is proportional to the electrons tunneling rate. The interpretation of the time resolved PL results is therefore straightforward and unambiguous. The DA signal is sensitive to changes in the electron and hole populations (which affect the bleaching of the absorption line) and to a build-up of local electric fields by space charge (which shifts the line). In that sense, when used in conjunction with the time resolved PL, DA provides a deeper insight into the dynamics of charge carriers in the system.

4.4 Experimental results.

The parameters of the three samples were chosen such that in the 50-Å sample, where $L_2 = L_1$, the condition $\Gamma_0/2 << \delta$ is satisfied, and we are in the weak relaxation regime. The 20-Å sample is chosen to be at the transition between the weak to strong relaxation, where $\Gamma_0/2 \approx \delta$. In the 10-Å sample, where $L_2 < L_1/2$, we are in the regime of strong relaxation, where $\Gamma_0/2 >> \delta$.

Fig. 4.4(a) displays a spectral DA measurement of the 50-Å sample. In this measurement the probe pulse is kept at a constant time delay of 4.2 ps with respect to the pump pulse and the laser energy is scanned. Two spectral features, 4 meV apart, are observed: a high energy peak, centered at 1.570 eV, and a lower one, centered at 1.566 eV. A similar line splitting is seen at the continuous wave PL of this sample (Fig. 4.4(b)). This line splitting is not observed in the DA and continuous wave PL measurements of the other two samples. It is associated with the splitting of the electronic levels in CQWs in the weak relaxation regime. Its absence in the other two samples confirms the predicted collapse of the splitting in the strong relaxation regime (section 4.2).

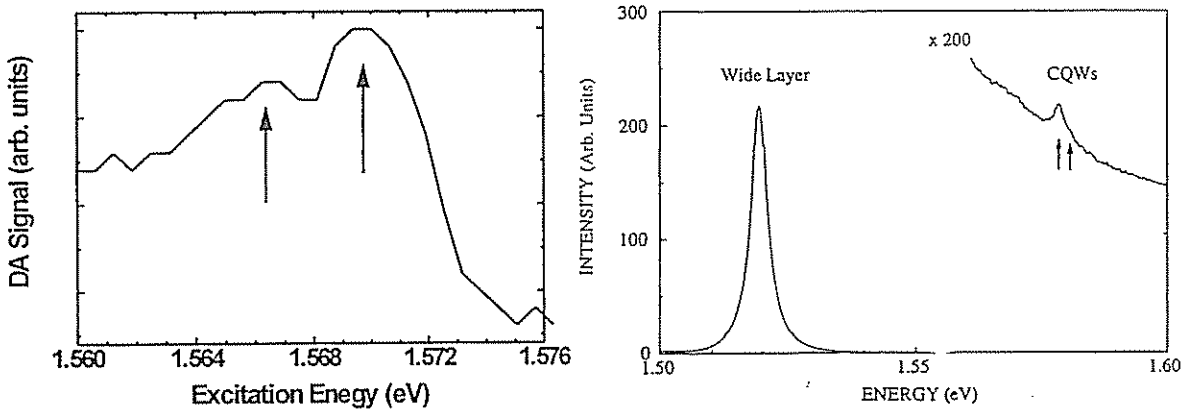

(a) (b)

Fig. 4.4: (a) DA spectrum of the 50-Å sample at a constant delay time of 4.2 ps. Arrows mark two well resolved peaks that decay with time constants of 36 ps (at 1.570 eV) and 7 ps (at 1.566 eV). (b) Continuous wave PL spectrum of the same sample. The shoulder at the high energy side of the CQWs luminescence is an evidence for the existence of a split energy level.

A PL spectrum of the 50-Å sample taken at a constant delay is shown in Fig. 4.5(a). Two peaks are observed: a large one at 1.520 eV and a small one at 1.570 eV. The first is associated with electron hole recombination in the 800-Å well (continuum), exhibiting a decay time of the order of 1 nanosecond. The higher energy peak is associated with the CQWs energy levels, and decays much faster. The same behavior is observed in all three samples. Fig. 4.5(b) shows the temporal evolution of the 1.570 eV luminescence line in

the three samples. It is seen that the decay time is very short, and depends on the thickness of L_2. The measured decay time decreases from 14 ps in the 50-Å sample to 3 ps in the 20-Å sample and then increases to 5 ps in the 10-Å sample. These results show very clearly that the decay rate varies *non-monotonically* with the coupling strength, and demonstrate the anomalous decay behavior of the system.

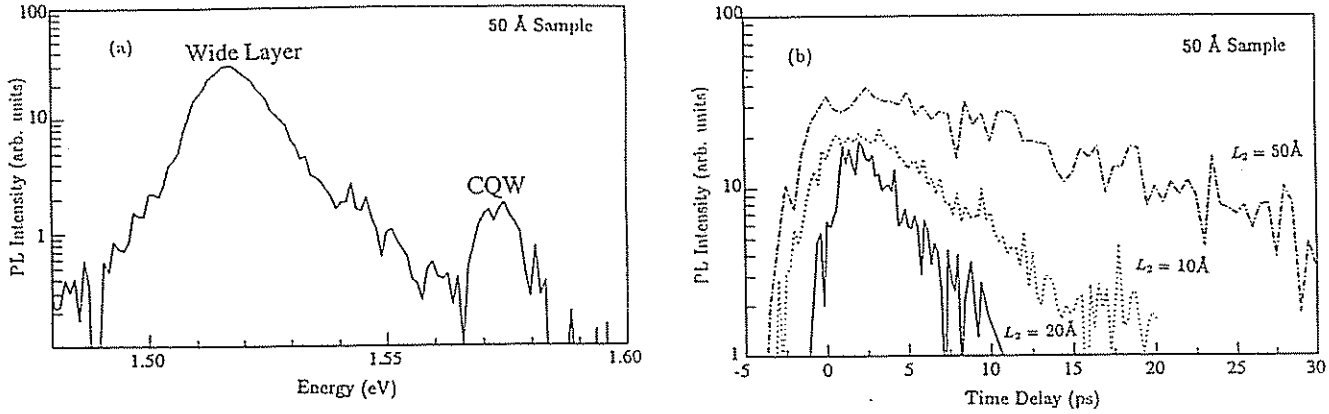

(a) **(b)**

Fig. 4.5: (a) PL spectrum of the 50-Å sample at a delay time of 10 ps. (b) Decay behavior of the CQWs PL in the three samples.

Let us turn now to describe the results of the DA measurements. In general, we can distinguish between contributions of electrons and holes to the DA signal. The electrons escape gives rise to a fast decaying signal (a few picoseconds decay time), while the holes escape is much slower and results in two contributions. One is a persistent signal, due to holes which didn't escape from the inner well during the time between two consecutive pulses. The DA experiments are performed at low power to minimize this effect. A second contribution of the holes is a slowly decaying signal (a few tens of picoseconds), coming from holes tunneling out from outer well. These different contributions are observed in Fig. 4.6(a). While the electrons relaxation results in a fast decay of the signal, the offset and the slow decay due to the holes are clearly seen. In the following we concentrate on the fast component and describe its decay in the three samples.

In the 50-Å sample each of the two spectral features observed in Fig. 4.4 decay at a different rate. The decay times of the low and high energy components are 7 and 36 ps, respectively.

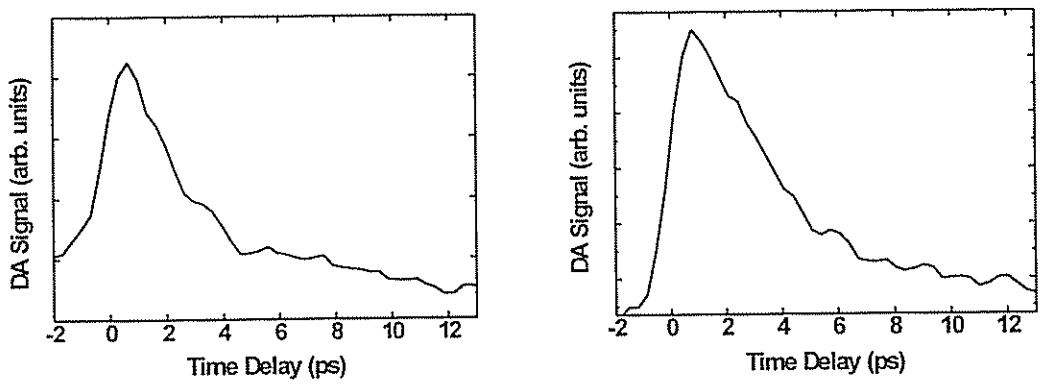

Fig. 4.6: Time resolved DA signals: (a) 20-Å sample and (b) 10-Å sample.

Turning to the 20-Å sample, the decay time of the fast (electron) component is 3 ps (Fig. 4.6(a)), and is constant throughout the excitonic line.

Fig. 4.6(b) gives the results of a temporal measurement for the 10-Å sample. A decay time of 7 ps is measured throughout the excitonic line. As found in the PL measurement - the observed decay time is longer than that of the 20-Å sample. It should be noted that the holes that are created in the outer well escape out immediately, and are not apparent in the DA signal.

We find therefore that the decay rates observed in the DA measurements are approximately the same as found in the PL experiment and the trend is preserved.

4.5 Discussion - the role of $\tilde{\Delta}$

We have shown that decay rate of CQWs to a continuum of states depends in a non-trivial way on the coupling strength between the two. In the weak relaxation limit the

decay rate increases with increasing the coupling strength. However, in the strong relaxation limit it decreases with increasing the coupling strength. We note that our temporal resolution does not enable us to resolve the fast component of the two exponential decay, which is calculated to be 40 fs in the 10-Å sample. We therefore measure the time evolution of the slower component only. Since the decay rate of this component scales like $1/\Gamma_0$, it is clear that in the 10-Å sample the measured time for the depletion of the system is expected to be longer then in the 20-Å sample. Indeed decay times of 7 ps and 3 ps were measured for the 10-Å and 20-Å samples, respectively.

It was assumed throughout this chapter that the energy levels mismatch, $\tilde{\Delta}$, can be neglected. In the following we wish to examine the validity of this assumption in view of the experimental results. In the 50-Å sample we have observed a different decay time for each spectral component (Fig. 4.4). The only parameter which can explain these different decay times (7 and 36 ps) is $\tilde{\Delta}$. The calculated energy shift, Δ_0, for the 50-Å sample is 0.06 meV, much smaller than $\Gamma_0 = 0.2$ meV and $\delta = 3$ meV. Such a small misalignment can not explain the observed large difference in the decay rate of the two spectral components. To fit the observed temporal behavior of the electrons in this sample to the theory one has to assume that $\tilde{\Delta} = -2.5$ meV. Well width fluctuations can be ruled out as the reason for this misalignment since this mechanism would have given an equal probability for positive and negative $\tilde{\Delta}$. A possible explanation is that in steady state the holes density is larger in the outer well due to Coulomb attraction to the electrons in the continuum. This results in lowering the electron energy level in the outer well and consequently in a slower decay time of the higher energy component. It should be emphasized, however, that the shortest measured decay time (7 ps) is shorter than the one that should have been measured in an ideal case, with a zero energy mismatch, and is, therefore, a low limit for it.

The behavior of the 20-Å sample critically depends on the exact values of the barrier height and thickness. For the 20-Å barrier the corresponding parameters are $\Delta_0 = -0.85$ meV, $\Gamma_0 = 4.4$ meV and $\delta = 3$ meV. Inserting these parameters into Eq. 4.2 we obtain a splitting of 2.3 meV between the electron levels and sub-picosecond decay of both levels. However, a slight decrease in the value of the barrier thickness (by one monolayer) would change the behavior into a two exponential decay, with a slow component of a few picoseconds, and a very fast sub-picosecond one. The absence of the splitting in this

sample and the observed decay of 3 ps could therefore be explained if we take the barrier thickness to be slightly less than 20 Å.

The calculated energy shift for the 10-Å sample, $\Delta_0 = -3.5$ meV, is rather large. Inserting it into Eq. 4.2, with the corresponding parameters, $\Gamma_0 = 40$ meV and $\delta = 3$ meV, we get 2 energy levels, 2.9 meV apart. However, the width of these levels is ~20 meV and ~0.1 meV, such that only the narrower one is observed. The decay time of the slow component is not very sensitive to the value of Δ_0, and the calculated decay time of 6.5 ps agrees well with our measurements.

Neglecting $\tilde{\Delta}$ is, therefore, a reasonable approximation in all the samples. Yet, The comparison of the experiment with the calculations while taking $\tilde{\Delta}$ into account, gives a deeper insight into the behavior of charge carriers in this system. Here, we exploit the advantages of the DA method that can monitor extrinsic processes such as holes tunneling and energy mismatch between the two symmetric wells.

5. Electron transport in the Stark ladder regime

5.1 Electron transport in a biased superlattice

We now turn to measure the electron motion in a superlattice subjected to external electric field. Three energy scales characterize this motion: Δ, the mini-band width, $\hbar/\tau_{scat}$, the level width, and eFd, the energy drop per period in the presence of an electric field. In good quality superlattices, having $\Delta > 10$ meV, the relation $\hbar/\tau_{scat} < \Delta$ is usually fulfilled. The relative size of eFd with respect to Δ and $\hbar/\tau_{scat}$ defines three regimes. The low field regime, where $eFd < \hbar/\tau_{scat}$, the high field regime, where $eFd \approx \Delta$, and an intermediate regime, where $\hbar/\tau_{scat} < eFd < \Delta$. The underlying physics of the electron transport in the low field regime is similar to that which prevails in bulk crystals, where the mobility is limited by impurity scattering. This is not the case at the high field regime. It was suggested by Tsu and Dohler that the transport in this regime can be modeled by phonon assisted hoping from one site to another.[13] The intermediate regime is the one which attracts most of the attention. In this range of applied fields the electron energy spectrum is characterized by discrete levels known as the Stark ladder. It was predicted by Esaki and Tsu that negative differential conductivity is to be observed in this regime.[12]

Several experimental works were devoted to the investigation of these transport regimes. It was demonstrated using time resolved PL that in the low field regime transport is made via extended Bloch states.[43] The experimental situation in the other regimes is more vague. Many experimental works, ranging from simple two probe transport measurements[14] to sophisticated application of microwaves, were made.[44] The experimental objective common to all these transport measurements is to determine the dependence of the average electrons velocity across the superlattice in the applied fields. Despite the intensive experimental work, the results are still ambiguous.[17]

Our goal was to address this problem using time resolved DA measurements and transmission spectroscopy. These are direct probes since the electron motion is time resolved and its energy spectrum can be monitored simultaneously by continuous wave spectroscopy. We start with an investigation of a Stark ladder formation using conventional continuous wave techniques as well as a novel differential method. We then present results of a time resolved DA measurements of the electron arrival rate to the electrodes and interpret these results in view of the evolution of the Stark ladder spectrum. We develop a mathematical model for the electron motion that fully

reconstructs our results. We then discuss them in the context of existing models of electron transport in superlattices.

5.2 The DA signal: origin and temporal evolution

The sample we studied is composed of 100 undoped 30 Å GaAs wells separated by 30 Å $Al_{0.3}Ga_{0.7}As$ barriers, in a p-i-n diode. The dominant contribution to the DA signal in the presence of an electric field results from space charge buildup in the doped regions, and is not a consequence of phase space filling. This behavior was studied by Livescu *et al.*[45] and was implemented to measure resonantly enhanced electron tunneling rates in coupled quantum wells,[46] and carriers sweep out rate from a single well.[47] The outline of the process is the following: a short laser pulse (pump) excites electron-hole pairs in the superlattice, in the intrinsic region of the diode. Carriers with opposite charges are swept in opposite directions in the electric field, and accumulate in the doped regions (Fig. 5.1). This accumulation of charges reduces locally the effective voltage between the electrodes, which in turn alters the absorption coefficient of the superlattice due to both quantum confined Stark effect[48] and Wannier Stark localization. The time dependent absorption change is the quantity measured by the probe pulse. The rate at which the magnitude of the differential absorption signal grows is, therefore, related to the accumulation rate of carriers in the doped regions. A fast voltage diffusion mechanism induced by a rearrangement of the charges in the electrodes reduces the local screening of the accumulated carriers at a rate which depends only on external parameters. The reduction of the local screening potential $V_s(t)$ is proportional to

$$V_s(t) \approx \frac{\tau_c}{t + \tau_c} \tag{5.1}$$

where $\tau_c \approx S_0 RC$ characterizes the voltage diffusion process and depends on the cross section of the light beam, S_0, the resistance per square, R, and the capacitance per unit area, C, of the diode.

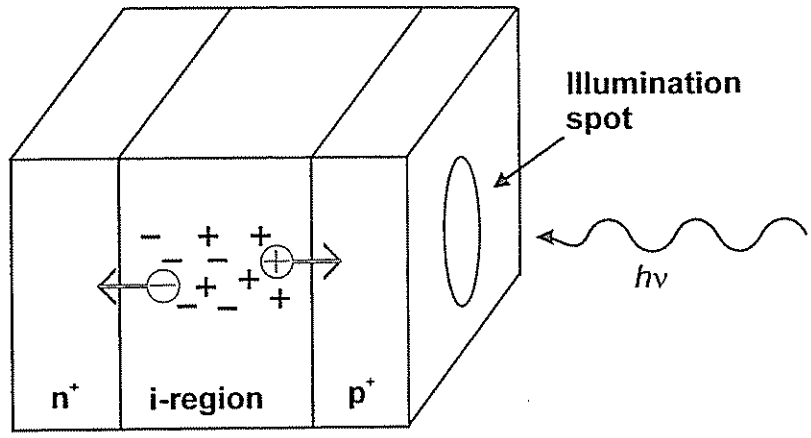

Fig. 5.1: The creation of space charge in a reverse biased superlattice: photo-excited holes (+) and electrons (-) are swept toward the p and n regions, respectively, creating a *local* screening potential at the cross section of the light beam.

5.3 Experiments

5.3.1 Stark ladder formation

The evolution of the energy spectrum at 7K, from band structure to complete localization, was monitored by measuring both transmission and photo-current, at different applied fields (Fig. 5.2). At a zero field, (i.e. external applied voltage which cancels the diode built in voltage) a mini-band absorption characteristic is observed, consisting of heavy and light hole excitonic peaks at wavelengths of 1.688 meV and 1.701 meV, respectively. At a field of 5×10^3 V/cm these excitons are field ionized and the peaks disappear. At higher fields, above 4×10^4 V/cm, clear Stark ladder peaks, whose spectral position depends linearly on the applied electric field, are observed. The actual field experienced by the superlattice is

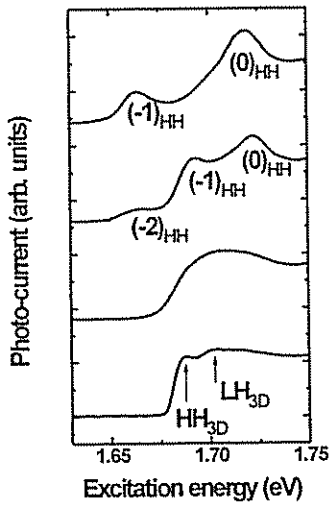

Fig. 5.2: Photo-current spectra at applied fields of (bottom) 0 V/cm, (middle low) 1.7×10^4 V/cm, (middle up) 5×10^4 V/cm, and (top) 8.7×10^4 V/cm.

extracted from the energy difference between the Stark ladder peaks. This extracted field is somewhat smaller than the one which is calculated taking into account the width of the nominally undoped regions as the intrinsic region. An additional electrically neutral region is formed, due to a freeze-out of holes in the p layer, increasing the actual width of the intrinsic region. From the blue shift of the absorption edge, which is equal to half the sum of the conduction and valence mini-band widths, we estimate the conduction mini-band width to be ~70 meV.

To achieve a better sensitivity to changes in the transmission spectrum as the Stark ladder evolves we applied spectral DA measurements. In this measurements the probe pulse is delayed by a constant value of 12 ps with respect to the pump pulse, and the DA signal is measured as a function of the excitation energy. As explained earlier, the pump pulses induce small changes, $V_s(t)$, in the applied voltage (Eq. 5.1). Therefore the probe measures a signal that is proportional to the derivative with respect to F, the applied field, of the absorption spectrum. Results at applied field of 8.7×10^4 V/cm are shown in Fig. 5.3, together with photo-current measurements taken at the same conditions. The two spectra correspond with each other according to the above interpretation.

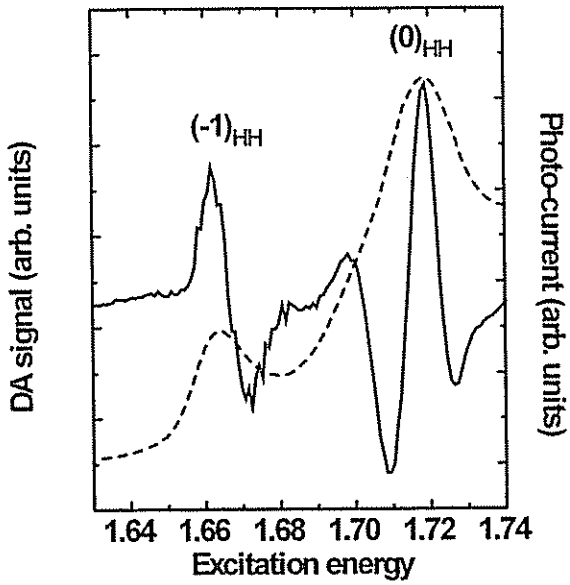

Fig. 5.3: DA spectrum at an applied field of 8.7×10^4 V/cm (solid line). Photo-current spectrum at the same applied field is given as a reference (dashed line).

This method of measurement exhibits a high spectral sensitivity due to its differential nature. We can follow the evolution of the Stark ladder over a much larger field range, than in the linear measurements: as low as 2.3×10^{4} V/cm, and as high as 1.1×10^{5} V/cm. The fan diagram in Fig. 5.4 summarizes the results of the spectral DA and the photo-current measurements. The DA peaks that corresponds to the $(-1)_{HH}$ and $(-2)_{HH}$ transitions are slightly shifted relative to the peaks that correspond to the same transitions in the linear measurements. This is because the differential signals result from a shift of the ladder stages. It can be noted that the light hole $(-1)_{LH}$ transition, which is masked by the heavy hole transitions at the linear measurements, clearly appears.

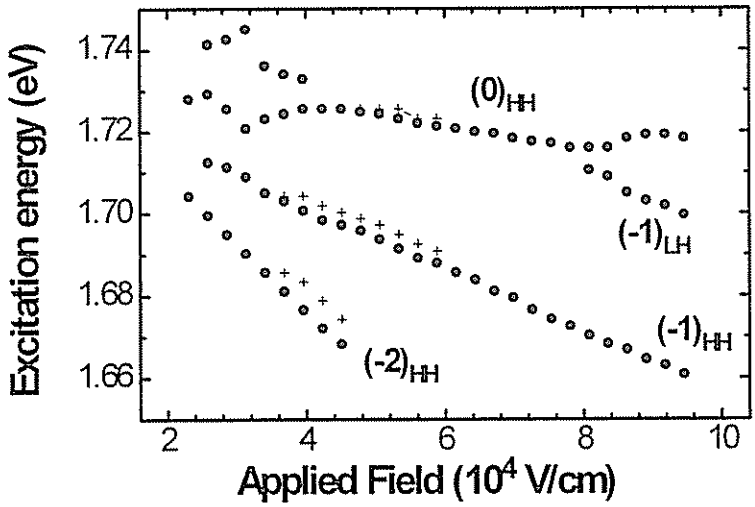

Fig. 5.4: A fan chart of superlattice transitions vs. applied field: crosses mark transitions measured by photo-current spectroscopy and solid circles - measured by spectral DA.

5.3.2 Time resolved measurements

We now turn to the time resolved DA measurements. A typical signal is shown in Fig. 5.5, where a rather fast rise followed by a relatively slow decay is observed. It should be emphasized, that the rise time is well within our temporal resolution and does not represent the pulse width. A summary of the rise times, which are related to the arrival

rate of electrons to the electrodes, at different applied fields and illumination powers appears in Fig. 5.6. At a field of 4×10^4 V/cm this rise time is approximately 10 ps. At higher fields the rise times become longer, up to 17 ps. At this field range discrete peaks appear in the optical spectra (transmission and photo-current), indicating that quantization of the energy spectrum occurs. At applied fields which are higher than $7-8\times10^4$ V/cm the rise times are shortened to a value of about 8 ps.

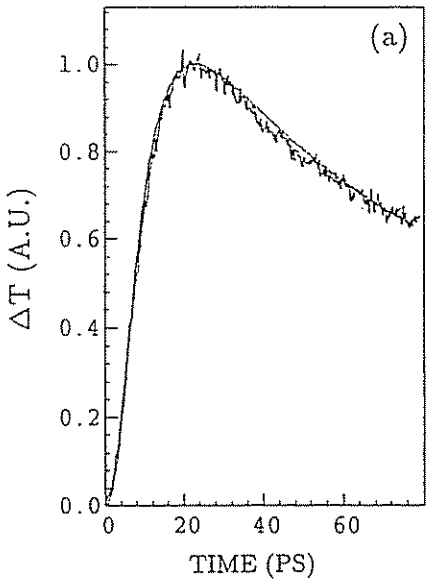

Fig. 5.5: Time resolved differential absorption signal measured at a field of 7.8×10^4 V/cm and its corresponding model fit (Eq. 5.2).

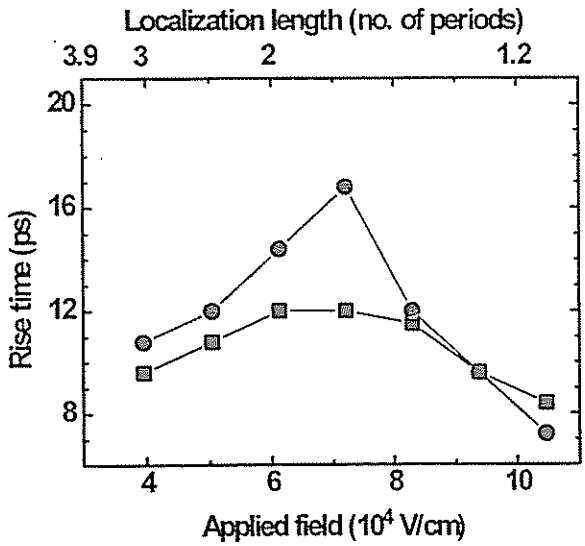

Fig. 5.6: Rise times of the temporal DA signals vs. applied field at illumination power densities of (solid circles) 0.7 W/cm and (squares) 5.9 W/cm. The lines are guides for the eyes.

The lowest illumination power at which we could get a reasonable signal to noise ratio was about 0.7 W/cm^2 , roughly equivalent to excitation density of 10^{15} pairs per cm^3 . We observed the same qualitative behavior as we increased the excitation densities over an order of magnitude, although the numerical values of the measured times are slightly intensity dependent. This is because at high excitation densities the charge accumulated in the doped regions at the beginning of the drift process can be large enough to reduce the effective field seen by electrons, which are still trapped in the wells of the superlattice. Since the holes are strongly localized already at very low fields, their contribution to the signal at very fast time scales can be neglected. We did not observe any effect of holes accumulation within the superlattice wells, which indicates that most of them escaped from the superlattice during the time between two consecutive pump pulses.

5.4 The electrons traversal times - quantitative models

Figure 5.6 clearly demonstrates that the escape time of the electrons from the superlattice is a non-monotonic function of the applied electric field. We interpret this behavior as a manifestation of the Wannier Stark localization. At low electric fields the mini-band breaks-up into discrete resonances (Wannier Stark ladder). As a consequence, the electrons mobility across the superlattice decreases with the electric field, and the measured escape time of the electrons increases. In that sense the electric field at which a differentiation of the Stark ladder peaks is optically possible marks the transition in the character of the electrons transport across the superlattice, from band transport to Stark localization. Above a certain field the Stark ladder states are close to a complete localization, and from that point on the dominant transport mechanism is tunneling into the higher band (continuum states above the barriers in our superlattice) and drift towards the electrodes. The tunneling probability increases with the electric field due to the decrease of the effective barriers height, and therefore the escape time decreases.

This interpretation of the field dependence of the rise times implies that the electrons dynamics at low and high electric fields is completely different. To give a more quantitative insight into the experimental data we have constructed a simple naive model, which describes the electrons motion in these two different regimes of applied field. In the high field regime barriers lowering, due to the increase of the applied field, is the reason for the faster escape times of the electrons. In this regime the electrons wave

function is localized in a very limited number of wells and their population in the wells decreases exponentially by tunneling, with a time constant τ_{tun}. As the electrons exit the wells they drift at a constant velocity towards the n doped region, where they generate a screening voltage $V_s(t)$ (Eq. 5.1). To fit the experimental data to this model we used the following expression for the magnitude of the absorption differential signal, which convolves the three processes mentioned above:

$$\Delta\alpha(\tau_d) \sim \int_0^{\min\{\tau_{tr},\tau_d\}} dt'' \int_0^{\tau_d} dt' \frac{\exp\left(-\frac{(t'-t'')}{\tau_{tun}}\right)}{1+\frac{\tau_d - t'}{\tau_c}}. \qquad (5.2)$$

τ_d is the time delay between the pump and the probe pulses, τ_{tun} is the tunneling time to the next mini-band, and τ_{tr} is the time it takes for an electron to drift across the whole superlattice. An example of fitted data is given in Fig. 5.5.

In principle, the drift velocity should have depended on the electric field via the mobility. The fitting procedure, however, yields a constant value of about 7-8 ps for τ_{tr}, at all the relevant fields (above 7×10^4). This implies that the drift is made at about saturation velocity. τ_c is found to be indeed sample dependent and constant over the whole range of applied fields. The tunneling time τ_{tun} was found to decrease as a function of the electric field from values of about 8 ps at a field of 6.8×10^4 V/cm to 3 ps at a field of 10^5 V/cm.

In the low field regime the voltage diffusion is modeled by the same τ_c dependence. However, the motion of electrons in the mini-band towards the doped region is diffusive. It is therefore assumed that the electrons move at a velocity, which is related to the electric field via the mobility, and is the mean value of a distribution which spreads linearly in time. The absorption change is modeled by the function

$$\Delta\alpha(\tau_d) \sim \int_0^{\min\{\tau_{tr},\tau_d\}} dt'' \int_0^{\tau_d} dt' \frac{\exp\left(-\frac{(t'-t'')^2}{4Dt''}\right)}{1+\frac{\tau_d - t'}{\tau_c}}, \qquad (5.3)$$

which keeps the notations already used in Eq. 5.2. τ_{tr} in this case is related to the drift velocity within the band, and D is a diffusion like coefficient which determines the rate at

which a Gaussian distribution spreads in time. This model yields mobility values which decrease from 300 $cm^2 / V \cdot sec$ at a field of 3.5×10^4 V/cm down to 100 $cm^2 / V \cdot sec$ at a field of 6.7×10^4 V/cm, marking the destruction of the band.

5.5 Summary and Discussion

To evaluate our results and to compare them with related works let us re-examine Fig. 5.6. To have some feeling for the data we added the localization length $\xi = \Delta / eF$ on the top x axis. The onset of localization, where the rise times start to increase with field, occurs at a field, in which the Stark ladder states are resolved in the optical spectra ($\sim 4 \times 10^4$). In order to resolve this states the energy separation between the peaks should be larger than their width, i.e. $eFd > \hbar / \tau_{scat}$. This is the same as the Esaki-Tsu criterion for the onset of negative differential conductivity.[12] In this sense our results qualitatively confirm their predictions. It should be noticed that the Esaki-Tsu model requires the existence of a band. This assumption is clearly incorrect when the localization length, ξ, is smaller than 3 wells. Yet we can see that negative differential conductivity (i.e. increase of rise times) persists up to $\xi \approx 1.5$ wells. At higher fields the tunneling to the next band become the dominant process. As a consequence there is no possibility of observing the predictions of the Tsu-Dohler model.

A year after the publication of our results, a similar work performed by Palmier *et al.*[49] was published. They applied a time resolved photo-current technique on a set of superlattices having different mini-band width. Their results were identical to ours showing a decrease in the electron velocity as the applied field is increased.

6. The excitonic interaction

The low energy side of the optical spectra of superlattices is usually marked by a sharp peak, originating from an exciton.[50] The Coulomb interaction between an electron and a hole in an exciton clearly complicates the simple one electron description of a superlattice that was presented in the previous chapter. The importance of the excitonic interaction is determined by the ratio between the exciton binding energy, E_b, and the inter-well coupling, $\delta/2$. In broad band superlattices, where $\delta/2 >> E_b$, as was the case in the previous chapter, it is justified to treat the excitonic interaction as a small perturbation. This assumption is not valid in narrow band superlattices, having $\Delta \leq 20$ meV ($\delta/2 \leq 5$ meV).

In this chapter we study the effect of the excitonic interaction on the energy spectrum and electron dynamics in a narrow band superlattice subjected to a normal electric field. We first present transmission and photo-current measurements exhibiting a unique evolution of the energy spectrum in the applied field. We then show results of degenerate FWM measurements and demonstrate that the oscillatory nature of the measured signals originates from excitonic quantum beats.

The superlattice we studied is composed of undoped 40 periods of 93 Å GaAs wells and 22 Å $Al_{0.45}Ga_{0.55}As$ barriers. The high and thin barriers, which separate the wells from each other, give rise to a narrow mini-band. A Kronig-Penney calculation yields a value of 8 meV for Δ, the mini-band width.

6.1 Continuous wave measurements

6.1.1 A modified Stark ladder

Figure 6.1(a) describes the photo-current spectrum at a nearly flat band condition. Three spectral features are clearly observed: two narrow and high peaks at 1.556 and 1.574 eV, labeled $(0)_{HH}$ and $(0)_{LH}$, respectively, and a broad feature centered at 1.563 eV, labeled $(\nu)_{HH}$. Upon the application of an electric field (Fig. 6.1(b)) the spectrum changes dramatically. While the $(0)_{HH}$ and $(0)_{LH}$ peaks broaden but remain at the same energy, the central feature splits into four peaks, which move away from each other with increasing field. The peaks at 1.556 and 1.574 eV are clearly the heavy and light hole

exciton transitions, respectively. This identification is based on their spectral position, relative strength and insensitivity to small applied fields. Each of these excitons is made of an electron and a hole, whose wave functions are localized in the same well. We shall show in the following that the $(\pm\nu)_{HH}$ peaks are associated with indirect excitons, each of which is formed of a heavy hole and an electron whose wave functions are localized in different wells. We also observe a set of similar transitions associated with the light hole. Their behavior is a replica of that of the heavy hole transitions and will not be discussed here.

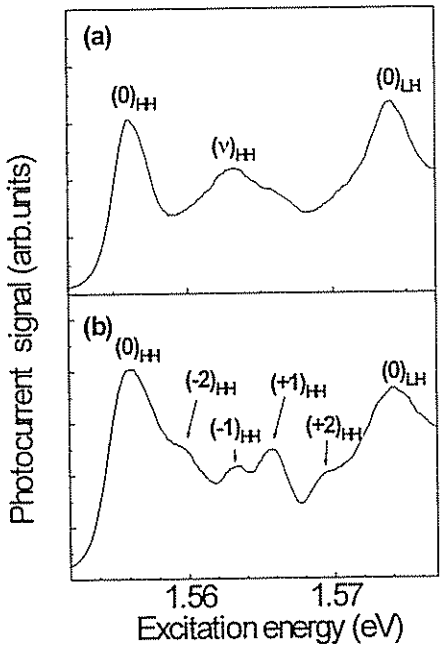

Fig. 6.1: Photo-current spectra at applied fields of (a) zero and (b) 1.7 kV/cm.

Fig. 6.2 summarizes the position of the $(\pm\nu)_{HH}$ peaks as a function of electric field in a fan chart. As can be seen, the general behavior resembles that of a Stark ladder in wide-band superlattices. Transitions labeled by a positive sign shift to high energies with increasing field, while those labeled by a negative sign shift to low energies. Furthermore, higher index transitions shift faster than lower index ones, and the $(0)_{HH}$ transition remains nearly stationary. The striking difference, however, is that at low fields ($F < 3$ kV/cm) the $(\pm\nu)_{HH}$ peaks appear at energies higher than that of the $(0)_{HH}$ transition. At higher fields the red shifting transitions, $(-\nu)_{HH}$, anti-cross the $(0)_{HH}$ transition: first the $(-2)_{HH}$, at an applied field of 3 kV/cm, and then the $(-1)_{HH}$ at 5

kV/cm. This anti-crossings are manifested in the photo-current spectra as an exchange of oscillator strength between two transitions (Fig. 6.3). This behavior is in contrast to the evolution of the spectrum of wide mini-band superlattices, where the $(-\nu)_{HH}$ transitions

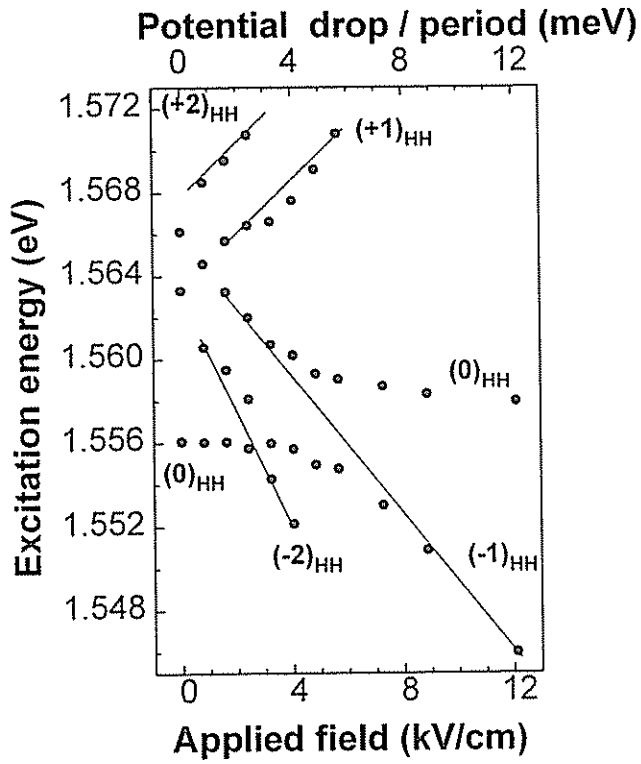

Fig. 6.2: A fan chart of superlattice transition energies vs. applied field.

are below the $(0)_{HH}$ one already at low fields (see for example Fig. 5.2 in the previous chapter).

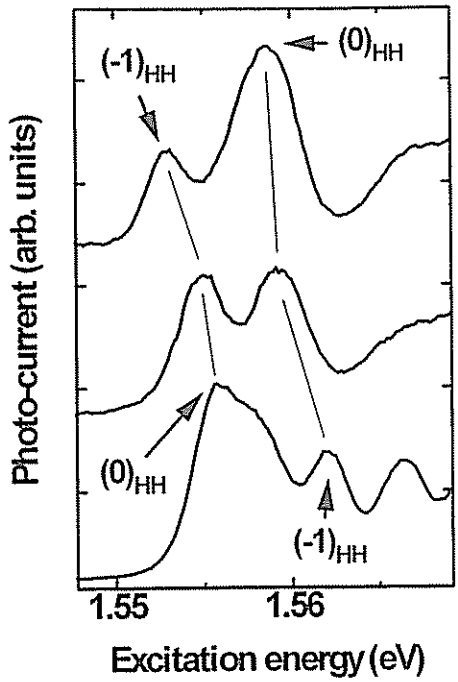

Fig. 6.3: Photo-current spectra at applied fields of (bottom) 1.6 kV/cm, (middle) 4.8 kV/cm, and (top) 7.2 kV/cm. In this field range the $(-1)_{HH}$ anti-crosses the $(0)_{HH}$ transition while exchanging oscillator strength.

6.1.2 A local tight binding model for the narrow band superlattice.

The evolution of the energy spectrum can be understood using a simple tight binding 5 wells model (Fig. 6.4). The major effect of the Coulomb interaction between the photo-excited electrons and holes is to deform the band structure locally. One can account for this interaction by taking the well depth to be space dependent, symmetric around the hole location. Thus, the energy level of an electron whose wave function is localized at the same well as the hole (the central well in the figure) would be lowered by the binding energy of a quasi-two dimensional exciton, ~8 meV. Similarly, the energy of an electron in an adjacent well will be renormalized by a lesser amount, the binding energy of an indirect exciton.

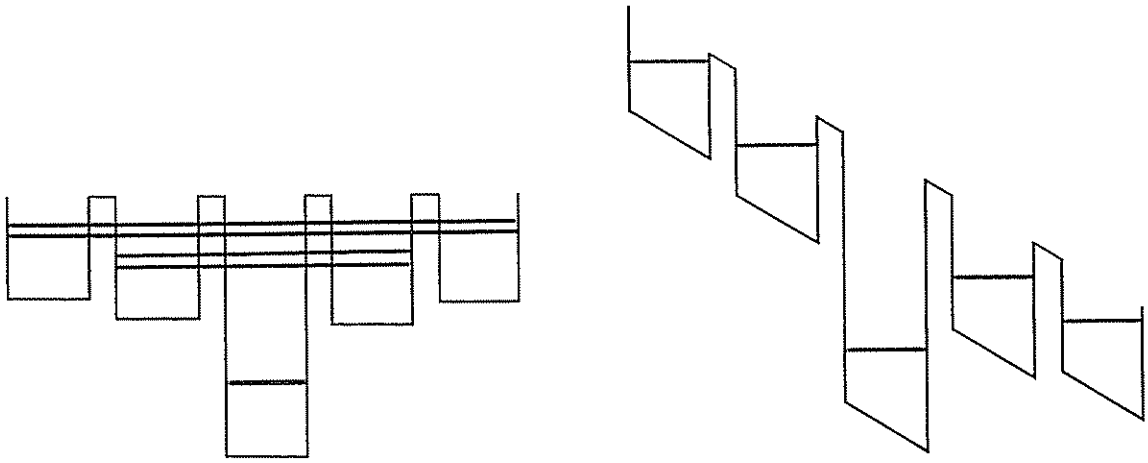

Fig. 6.4: Illustrations of the tight binding five wells model: (a) at a flat band condition and (b) at an applied field that corresponds to ~2 kV/cm.

Using this model we can modify Eq. 1.6 and write ε_ν, the energy of an electron whose wave function is centered in the ν-th well in the presence of an electric field, as

$$\varepsilon_\nu = E_1 - E_B^{(\nu)} + \nu eFd \qquad \nu = 0, \pm 1, \pm 2, \ldots \tag{6.1}$$

where E_1 is the confinement energy in a well, $E_B^{(\nu)}$ is the excitonic binding energy between a hole positioned in the 0-th well and an electron centered in the ν-th one, F is the applied field and d is the superlattice period. It should be noticed that $E_B^{(\nu)}$ is nearly independent of the field because the electron wave function is already localized at zero applied field and changes only a little as it is increased.

Although this tight binding model is rather simple it provides a clear physical insight into the observed optical spectra. At a flat band conditions the energy levels are symmetric with respect to the central well. The effect of tunneling is to split the degenerate energy levels $\varepsilon_{\pm\nu}$ into a symmetric and an anti-symmetric levels which are very close in energy. The broad spectral feature $(\nu)_{HH}$ in Fig. 6.1(a) is associated with transitions to these levels. Upon application of an electric field this symmetry is broken, and the energy levels $\varepsilon_{-\nu}$ shift to low energies while the $\varepsilon_{+\nu}$ shift to high energies. At certain fields, when the applied field compensates for the binding energy differences

between neighboring sites, we get degeneracy of energy levels. These are responsible for the observed anti-crossings.

6.2 Time resolved measurements

6.2.1 Four wave mixing

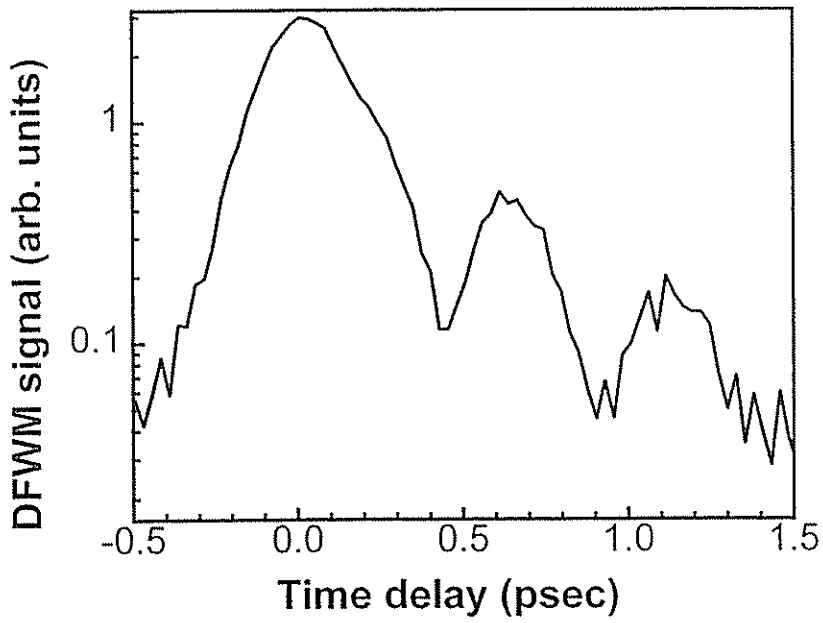

Fig. 6.5: Time resolved FWM signal (on logarithmic scale) at an applied field of 9.7 kV/cm and excitation energy of 1.551 eV.

Figure 6.5 shows a typical FWM signal (on logarithmic scale) measured on a biased superlattice. Three oscillations are clearly seen having a period of 0.5 ps. These oscillations are damped with a dephasing time of 0.35 ps. Examining the oscillation frequencies at various fields we find a clear dependence on the applied field. This is demonstrated in Fig. 6.6, where we show the oscillation frequency, $\hbar\omega$, as a function of applied field, at an excitation energy of 1.559 eV. Two regimes are clearly observed. The first is below 2 kV/cm and is characterized by high frequency oscillations, between 6.5 to 9 meV. The second regime is above 3.5 kV/cm and the frequencies are lower,

between 4.5 to 7.5 meV. In both regimes the oscillation frequency increases monotonically with field. In the intermediate field range the oscillations are less pronounced and their pattern is complicated, consisting of non regular low amplitude oscillations.

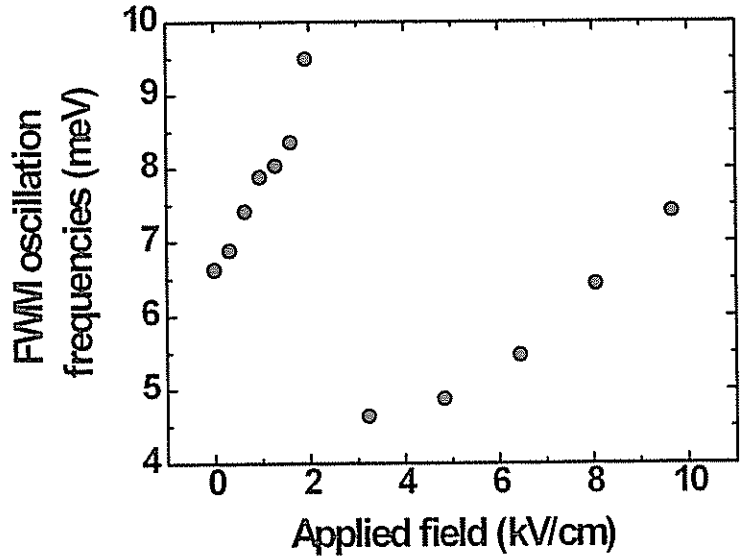

Fig. 6.6: FWM oscillation frequencies vs. the applied field at an excitation energy of 1.559 eV.

6.2.2 Exciton quantum beats

In view of the fact that we see oscillations, whose frequency depends linearly on the applied field, one might draw a conclusion that these are Bloch oscillations. However, our tight binding model suggests that these oscillations have a *local* nature, and are quantum beats between the various Stark ladder transitions.

To examine this interpretation we study the dependence of the oscillation frequency on the excitation energy. Figure 6.7(a) describes two FWM signals measured at different excitation energies and the same applied field of 3.2 kV/cm. It can clearly be seen that the oscillation period varies with the excitation energy. At high excitation energy (1.562 eV, lower curve) the period is 0.9 ps while at low energy (1.551 eV, upper curve) the period is longer, 1.3 ps. Fig. 6.7(b) describes the energy levels (within the 5 wells model) and illustrates the origin of the different oscillation periods. At this applied field the

$(-2)_{HH}$ transition has already crossed the $(0)_{HH}$ one while the $(-1)_{HH}$ transition is above it (see also Fig. 6.2). By tuning the laser to a higher energy it covers only the $(0)_{HH}$ and the $(-1)_{HH}$ transitions, and we excite a superposition of the two. Thus, the quantum beats are associated with electron states in adjacent wells. Shifting the excitation energy to the red the laser spectrum no longer overlaps with the $(-1)_{HH}$ transition but rather with the $(-2)_{HH}$. In that case the quantum beats involve electron wave functions which are centered two wells away from each other.

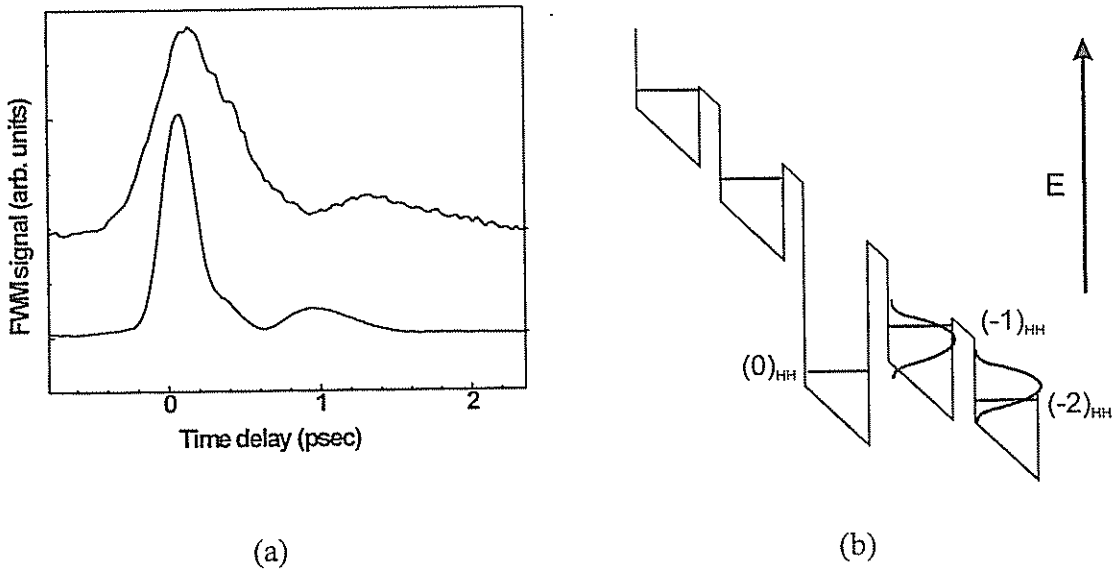

(a) (b)

Fig. 6.7: (a) Time resolved FWM signals at excitation energies of (top) 1.551 eV and (bottom) 1.562 eV. (b) The corresponding five wells model for the photo-excited energy levels.

Similarly, the two oscillation regimes of Fig. 6.6 can be associated with quantum beats. We can trace the transitions involved using the fan chart of Fig. 6.2. In the low field regime the transitions involved are the $(0)_{HH}$ and the $(+1)_{HH}$. As can be seen in Fig. 6.1(b), the $(+1)_{HH}$ is the transition with the highest oscillator strength. Furthermore, it shifts away from the $(0)_{HH}$ transition with increasing field at a rate which agrees with the measured frequency. Similar considerations lead us to associate the high field oscillations with quantum beats between the $(-1)_{HH}$ and the $(0)_{HH}$. The transition from $(+1)_{HH}$ to $(-1)_{HH}$ oscillations can be very well explained within the simple model presented above. A straightforward tight binding calculation at low fields shows that the wave function of an electron associated with the $(+1)_{HH}$ transition has the largest overlap

with the hole. Therefore, this transition has the largest oscillator strength and dominates the observed oscillations. At high fields, the $(-1)_{HH}$ gains oscillator strength due to the anti-crossing with $(0)_{HH}$.

We wish to remark here that the behavior at a nearly flat band ($F < 1\text{kV/cm}$) is different and the FWM signal is not oscillatory. This behavior will be discussed in more detail in the next chapter.

6.3 Summary and discussion

No experimental research was performed on narrow band superlattices prior to this work. In Ref. [51] there is a theoretical analysis of an extremely narrow band superlattices (100 Å barriers) and indeed the energy dependence of the different Stark ladder states is similar to our experimental results.

Parallel to this work, field dependent oscillations were observed in a FWM experiment in a GaAs/AlGaAs superlattice and were attributed to the phenomenon of Bloch oscillations.[25] Later, sub-millimeter wave emission from a superlattice under the same condition was attributed to the same phenomenon.[26] Our work puts a question mark on this conclusion and suggests that FWM field dependent oscillatory signals originate from excitonic quantum beats. Following the submission of this work to publication some of the authors of Ref. [25] published a theoretical work that postdicted our linear results. Furthermore, they claimed that there is a difference in the physical origin, hence in the frequency, of the two oscillatory signals (of Refs. [25] and [26]). They suggest that the FWM signal is, indeed, of excitonic origin and claimed that the electromagnetic wave emission is a true mark of Bloch oscillations.[28] To date, no experimental evidence has supported these results.

7. Fano interference in a parallel magnetic field

A magnetic field is frequently used in the investigation and characterization of superlattices (see section 1.3). Following the theme of this work we are interested in parallel magnetic fields where the cyclotron motion of the electron interfere with tunneling across the superlattice barriers. In this chapter we wish to study the energy spectrum and dynamics of excitons in the strong magnetic field limit. As explained in the introduction this limit is reached when the cyclotron energy, $\hbar\omega_c$, is larger than the mini-band width. For narrow band superlattices it can be achieved using available magnets.

We show that the optical spectrum can be correctly understood only if interference effects between direct and indirect excitons and their continua are considered. The interaction between a continuum of states and a discrete resonance is known to give rise to a unique absorption spectrum[52]. When such a system is excited from a common ground state, interference of the transition amplitudes of the resonance and the continuum occurs. This results in an asymmetrical peak in the absorption line-shape with a vanishing absorption on one of its sides. This phenomenon was studied by Fano and is found in atomic systems,[53] Bulk semiconductors[54,55] and low dimensional structures[56]. It was recently shown that Fano interference could have a profound effect not only in the spectral domain but also in the dynamics of the system.[57]

In this chapter we focus on the interference between the $(\pm 1)_{HH}$ excitonic transitions, from a hole state in a certain well to electron states in adjacent wells and the continuum of the $(0)_{HH}$ exciton, hereafter designated by $(0)_{HH}^{cont}$. By varying the strength of the magnetic field we are able to tune the energy of the $(\pm 1)_{HH}$ indirect exciton relative to the edge of $(0)_{HH}^{cont}$. We then drastically vary the coupling between the discrete $(\pm 1)_{HH}$ transition and this two dimensional continuum of states. This provides a unique opportunity to investigate Fano interference near the band edge. We find that both the decay pattern of the FWM signal and the linear transmission spectra change as the $(\pm 1)_{HH}$ resonance crosses the continuum edge, $(0)_{HH}^{cont}$. The FWM signal abruptly develops an oscillatory behavior and the absorption peak of the $(\pm 1)_{HH}$ transition, starts to shift rapidly to higher energies.

This chapter is organized as follow: in section 7.1 we review excitonic transitions in superlattices subjected to strong magnetic fields and the phenomenon of Fano interference. in section 7.2 we describe transmission and FWM experiments.

Interpretation of the results and a quantitative model of Fano interference for our system is given in section 7.3.

7.1 Introductory review

7.1.1 Exciton in a superlattice subjected to a parallel magnetic field.

The dispersion curves of an electron in a superlattice subjected to a parallel magnetic field were discussed in the introduction (section 1.3) and can be drawn as in Fig. 7.1(b). To include the Coulomb interaction between the electron and hole we first turn off the magnetic field. Following arguments in the previous chapter (section 6.2.2), the excitonic states in the absence of magnetic field can be drawn as in Fig. 7.1(a).

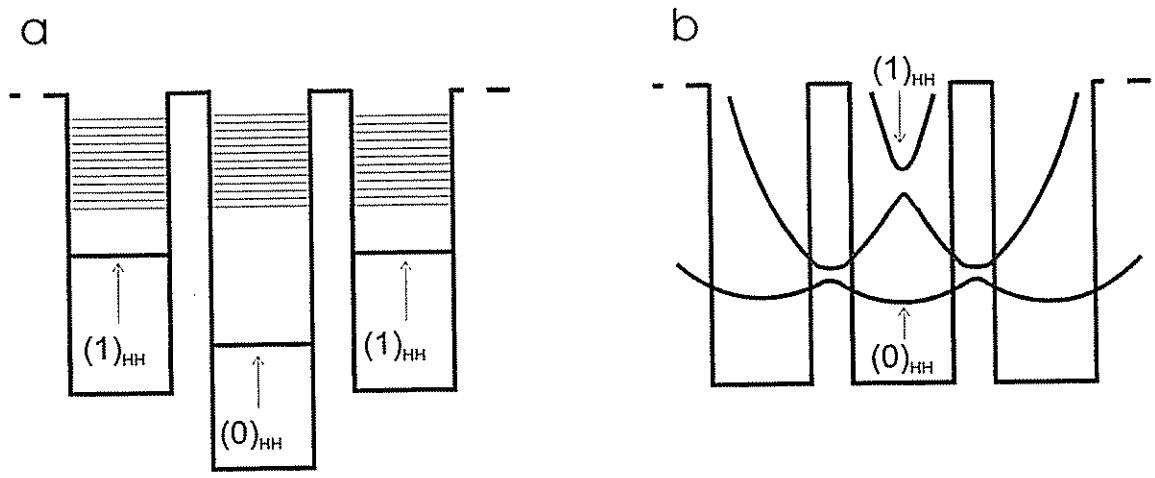

Fig. 7.1: The electron energy levels in a narrow band superlattice (a) in the presence of a hole and (b) in the presence of a strong magnetic field. $(0)_{HH}$ and $(\pm 1)_{HH}$ designate the electron levels that are involved in the direct and indirect excitons, respectively.

To understand the energy spectrum of excitons in a strong magnetic field let us first turn off the Coulomb interaction. It can be easily shown that to a first order in perturbation theory the magnetic field changes the electron wave function (Eq. 1.9) only in the normal direction (z direction), while maintaining its plane wave nature in the layers. It follows, that the description of exciton creation from 2D continuum states in

quantum wells[1] can be applied directly to superlattices in the strong magnetic field limit. Excitons are formed, then, by electrons whose guiding centers are at the extrema of the dispersion curve marked by arrows in Fig. 7.1(b). The electrons related to the lower extremum are located in the central well and are responsible for the creation of the direct intra-well $(0)_{HH}$ exciton. The electrons at the higher extremum reside primarily at the left and right wells and form the indirect exciton $(\pm 1)_{HH}$.

The energy of the $(\pm 1)_{HH}$ extremum is determined by the intersection point of two parabolas centered in the right and left wells (Fig. 7.1(b)). It is clear from Eq. 1.10 that increasing the magnetic field will cause this intersection point to shift to higher energies. Since the diamagnetic shift is the same for all states, the magnetic field shifts the indirect exciton energy upward relative to the continuum edge (the bottom of the central parabola). Consequently, at some critical field the $(\pm 1)_{HH}$ energy crosses the edge of the $(0)^{cont}_{HH}$. We define by Ω the difference in energy between the $(\pm 1)_{HH}$ and the edge of the $(0)^{cont}_{HH}$:

$$\Omega = E[(\pm 1)_{HH}] - E[\text{edge of } (0)^{cont}_{HH}] \tag{7.1}$$

It follows that at zero magnetic field $\Omega < 0$, and at the critical field, where the $(\pm 1)_{HH}$ crosses the $(0)^{cont}_{HH}$ edge, $\Omega = 0$. From Fig, 7.1(a) it can be seen that $\Omega = 0$ occurs at a magnetic field which shifts the $(\pm 1)_{HH}$ by its binding energy.

7.1.2 Fano interference

The excitation into a superposition of a discrete state ($(\pm 1)_{HH}$ in our system) and a continuum of states ($(0)^{cont}_{HH}$) was studied by Fano:[52] In his analysis he represents the matrix element for optical excitation from a common ground state, $|i\rangle$, into the superposition state, $|\Psi(E)\rangle$, as:

$$\langle \Psi(E)|\mathcal{D}|i\rangle = \frac{1}{\pi V_E^*}\langle \Phi^e{}_{exc}|\mathcal{D}|i\rangle \sin\Theta + \frac{1}{\pi V_E^*} P\int dE' \frac{V_{E'}\langle \Phi^e{}_c(E)|\mathcal{D}|i\rangle}{E-E'}\sin\Theta - \langle \Phi^e{}_c(E)|\mathcal{D}|i\rangle\cos\Theta \tag{7.2}$$

where $\Theta = -\arctan \pi|V_E|^2/[E - E_{exc} - f(E)]$ and $f(E) = P\int dE'|V_{E'}|^2/(E-E')$. $\mathcal{D}$ is the excitation operator, V_E is the energy dependent coupling term between the discrete $\Phi^e{}_{exc}$

state and a continuum $\Phi^e{}_c(E)$ state, E_{exc} is the energy of the discrete level, E is the excitation energy, and P stands for the principal value of the integral. $\langle \Phi^e{}_{exc}|\mathcal{D}|i\rangle$ and $\langle \Phi^e{}_c(E)|\mathcal{D}|i\rangle$ are the excitation matrix elements into uncoupled discrete and continuum states, respectively. Note that $\sin\Theta$ and $\cos\Theta$ are even and odd functions of $E - E_{exc} - f(E)$, respectively. Consequently the first two terms in Eq. 7.2 have an opposite phase relative to the third term around the sharp resonance at $E = E_{exc} + f(E)$. This is manifested as an asymmetrical line shape in the absorption spectrum that characterizes a Fano resonance.

7.2 Experiments

7.2.1 Transmission spectroscopy

The sample we used is the same as in the previous chapter. The exact growth parameters appears in appendix A. In Fig. 7.2 we present three transmission spectra measured at 1, 3, and 6 Tesla. The two strong peaks at 1.556 and 1.574 eV are the heavy and light hole exciton transitions, respectively. The third smaller peak at the intermediate value of 1.563 eV at 1 Tesla is the indirect exciton transitions. The main contribution to this feature is from the $(\pm 1)_{HH}$ transition.

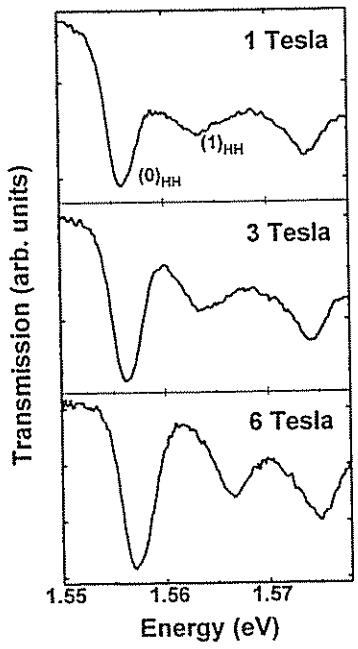

Fig. 7.2: Transmission spectra at magnetic fields of 1,3, and 6 Tesla applied parallel to the layers.

It can be seen that while the positions of the direct heavy and light hole excitons shift only slightly between 1 and 6 Tesla (less than 1 meV), The $(\pm 1)_{HH}$ peak exhibits a much larger shift (~3 meV). The open circles in Fig. 7.3 describe the energy of the indirect exciton (relative to the *direct* one) as a function of the magnetic field. We observe a profound change around 3 Tesla: while at low fields the relative position of the indirect exciton remains constant, it shifts quadratically above 3 Tesla. The solid line in Fig. 7.3 describes the calculated energy difference between the indirect and direct excitons based on Eq. 1.10. It can be seen that there is a very good agreement with the measured data points above 3 Tesla. The curvature of the line is determined by fundamental constants and the only adjustable parameter is the energy difference at $B = 0$, which is taken as 5.5 meV. Clearly this line fails to describe the field dependence below three Tesla.

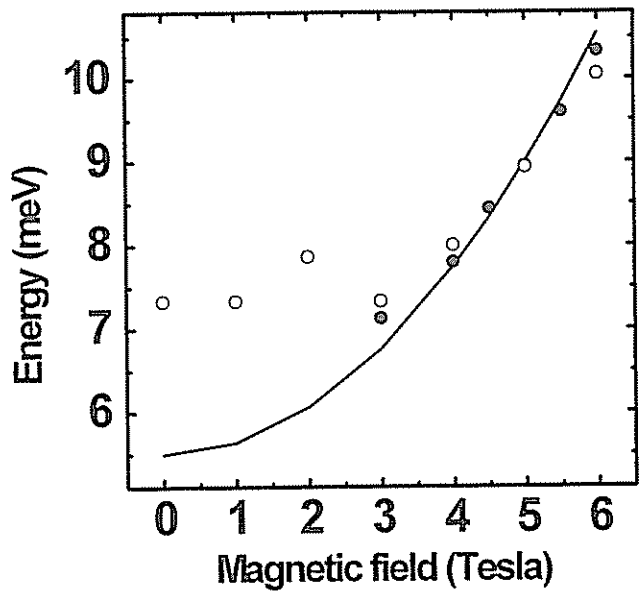

Fig. 7.3: The energy difference between $(0)_{HH}$ and $(\pm 1)_{HH}$ vs. applied magnetic field: solid line - calculated, open circles - measured. The solid dots are the measured FWM frequencies.

7.2.2 FWM experiment

Fig. 7.4 shows FWM signals measured at different applied magnetic fields with the excitation energy centered at 1.559 eV, covering both the direct and indirect transitions. A qualitative difference between the low and high field signals is clearly observed. Below 3 Tesla the overall decay is exponential, exhibiting a dip near zero time delay. An abrupt change in this behavior occurs at $B \geq 3$ Tesla: fast oscillations appear in the decay pattern. The frequency of these oscillations increases quadratically with magnetic field, as shown in Fig. 7.3 (solid dots). It can be seen that this frequency matches the energy difference between indirect and direct excitons (open circles). One can, therefore, conclude that the fast oscillations are quantum beats between the indirect and direct excitons.

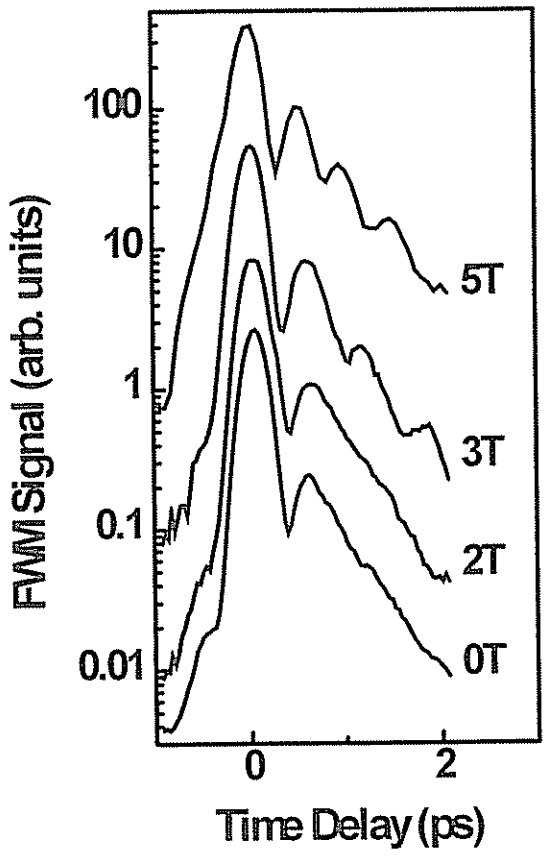

Fig. 7.4: FWM signals vs. time delay at different applied magnetic fields. The laser is centered at 1.559 eV.

7.3 Interpretation

We now wish to discuss the experimental results. We start with the linear transmission data and show that it can be understood in terms of the interaction between a resonance and a continuum. This interaction causes each continuum state to be repelled from the resonance by an amount which depends on their relative energy separation. Consequently, there is a "pile-up" of continuum states and a sharp absorption peak is formed. At $\Omega < 0$, as the resonance is far below the continuum edge, the interaction is weak and effectively involves only the lowest continuum states. The resulting "pile-up" is not pronounced and the energy of the absorption peak is not very sensitive to small changes in the energy of the discrete level. When Ω becomes positive the interaction is enhanced and involves more continuum states. The absorption resonance becomes sharper and more sensitive to changes in the energy of the discrete state. This mechanism explains qualitatively the trends observed in the absorption line-shapes (Fig. 7.2): blue shift and narrowing of the $(\pm 1)_{HH}$ peak. It also explain the different shift rates of the $(\pm 1)_{HH}$ exciton below and above 3T (Fig. 7.3).

7.3.1 Fano interaction between a two dimensional continuum and an exciton

To make the above interpretation more quantitative let us now turn to examine the Fano interaction in the case of our superlattice. We consider a 1S indirect exciton whose electron is coupled by tunneling to a two dimensional continuum of states. The electron part of the indirect exciton wave function is written as $\Phi^{e}_{exc} = \varphi^{e}_{exc}(z)\exp(-k_{||}r)$ and the 2D continuum state is approximated as $\Phi^{e}_{c} = \varphi^{e}_{c}(z)\exp(-ik_x x - ik_y y)$. The matrix element for tunneling between these two states has, therefore, the form

$$\left\langle \varphi^{e}_{exc}(z)\middle|\nu\middle|\varphi^{e}_{c}(z)\right\rangle \left\langle \exp(-k_{||}\cdot r)\middle|\exp(-ik_x x - ik_y y)\right\rangle \qquad (7.3)$$

where ν is the tunneling operator. The left bracket in Eq. 7.3 can be approximated as a constant [58] and estimated to be $\tilde{V} \approx 4$ meV in our structure. The important quantity in Eq. 7.2 is the coupling term, V_E, that characterizes the physical interaction between the discrete state and the continuum. Taking into account the 2D density of states and energy conservation, we find:

$$V_E = \frac{2VR_y}{\left(E^2 + R_y^{\,2}\right)^{\frac{3}{2}}} \tag{7.4}$$

where $R_y = \hbar^2 k_{||}^{\,2} / 2m^*$ is the indirect exciton Rydberg. Note that the use of plane waves rather than the radial wave functions to describe the continuum states leads to an over estimation of the coupling strength just above the continuum threshold at $E = 0$. Therefore this approximation gives an upper limit for the value of V_E.

7.3.2 Comparison with experiments

We now insert V_E into the Fano formula (Eq. 7.2) and calculate the absorption line-shape. Fig. 7.5 describes the evolution of the calculated absorption spectrum as we vary Ω. One can see the formation of a narrow resonance, which shifts to higher energies with increasing Ω, forming a shallow dip on its low energy side. Note that this shift is not linear in Ω. It is nearly insensitive to changes in Ω for $\Omega < 0$ and it follows the energy of the discrete level more accurately at $\Omega > 0$.

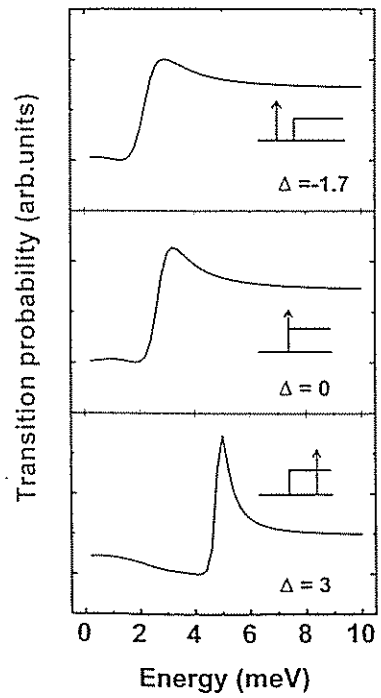

Fig. 7.5: Calculated Fano interference line-shapes at 3 different values of Ω. Insets: energy position of the discrete level (arrow) relative to the continuum edge.

The above model implies that the absorption peak is not the bare $(\pm 1)_{HH}$ but is rather a mixture of this resonance and the $(0)_{HH}^{cont}$. At low fields it has predominantly a continuum nature and at high magnetic fields this peak contains a larger excitonic contribution.

This mixed nature of the indirect exciton peak is consistent with the different decay patterns of the FWM signal below and above 3 Tesla. We note that in the FWM experiment we excite simultaneously the $(0)_{HH}$ exciton and the $(\pm 1)_{HH}$ peak. Since FWM is a coherent process the resulting signal will contain a contribution due to interference between the two transition amplitudes. The character of the $(\pm 1)_{HH}$, being continuum or exciton like, determines the type of this interference: either between a resonance ($(0)_{HH}$) and a continuum or between two resonances.

To examine the FWM data in view of this interpretation, we consider first the low field signal. It was shown by Feldmann *et al.* that when an excitonic resonance and its continuum are co-excited in a FWM experiment, the resulting decay pattern is exponential with a dip just after zero time delay.[59] This pattern is similar to the one observed in our experiment below 3 Tesla. We can therefore conclude that in this field range the $(\pm 1)_{HH}$ has a *continuum nature*. As we increase the magnetic field the signal changes into quantum beats between two resonances. This implies that the $(\pm 1)_{HH}$ peak contains a larger *excitonic contribution*. It should be noticed that the first minimum in the oscillatory signal is deeper than the others. This is due to the fact that the contribution of the continuum states to the absorption peak is not negligible.

7.4 summary

A pre-requisite for observing a Fano resonance is to achieve a degeneracy between a discrete level and a continuum of states. Coupled wells systems and superlattices seem to be natural candidates for exhibiting this phenomenon. To date, however, there is no report on the observation of Fano interference in these structures. The main obstacle is that these systems are complex and the interference is masked by other processes (i.e. relaxation processes, changes in the tunneling parameters etc.). The application of a parallel magnetic field on a narrow band superlattice enables us to tune the discrete level while keeping all other parameters from being modified too severely. We could, therefore, identify and investigate the Fano interference in a simplified system.

It should be pointed out that time resolved spectroscopy has proven to be a powerful tool in the investigation of interference phenomena. Although the Fano interference is

manifested in the linear spectral, the abrupt appearance of oscillations in the FWM decay pattern is more striking. The reason for this abruptness is not clear and a better theory is needed.

8. Summary

In this research we have implemented time resolved and continuous wave optical spectroscopy to study dynamics of carriers in superlattices. We have used external magnetic and electric fields, together with the ability to design and grow our superlattice samples, to perform a controlled study of specific processes in these structures.

We introduced some modifications to the simple 1D picture that is commonly applied in the investigation superlattices. Firstly, considering the 3D Coulomb interaction, we showed that the excitonic interaction substantially deform the ordered Stark ladder spectrum and the FWM response of narrow band superlattices. Secondly, investigating the coupling of discrete levels to a 2D continuum, we identified and investigated the Fano interference demonstrating during this research the high sensitivity of the non-linear FWM method. The coupling of CQWs system to a 3D continuum was studied as well, leading to the observation of a nonmonotonic dependence of the relaxation rate in the coupling strength.

The ability of optics to perform spectral measurements simultaneously with time resolved measurements, enabled us to contribute to the relatively well studied subject of transport across a superlattice. We could relate the formation of a Wannier Stark discrete spectrum with the transport properties of electrons and obtain a good understanding of the underlying physical processes.

9. References

1. G. Bastard, *Wave mechanics applied to semiconductor heterostructures,* les editions de physique, (1988).
2. see e.g. E Merzbacher, *Quantum Mechanics*, John Wiley, (1961).
3. *Physics and Applications of Quantum Wells and Superlattices* ed. E. E. Mendez and K. von Klitzing, NATO ASI Series B, Vol 170, Plenum Press (1987).
4. J. Bleuse, G. Bastard, and P. Voisin, *Electric-Field-Induced Localization and Oscillatory Electro-optical Properties of Semiconductor Superlattices,* Phys. Rev. Lett. **60**, 220 (1988).
5. S. Adachi, *GaAs, AlAs, and $Al_xGa_{1-x}As$: Material parameters for use in research and device applications,* J. Appl. Phys. **58**, R1 (1985).
6. G. H. Wannier, *Elements of Solid State Theory,* Cambridge University Press, (1960).
7. J. Zak, *Stark Ladder in Solid?,* Phys. Rev. Lett. **20**, 1477 (1968).
8. A. Rabinovitch and J. Zak, *Electrons in Crystals in a Finite Range Electric Field*, Phys. Rev. **B4**, 2358 (1971).
9. W. Shockley, *Stark Ladder for Finite, One-Dimensional Models of Crystals*, Phys. Rev. Lett. **28,** 349 (1972).
10. D. Emin and C. F. Hart, *Existence of Wannier Stark localization,* Phys. Rev. **B36**, 7353 (1987).
11. J. Iafrate, J. B. Krieger, and Yan Li, in *Electronic Properties of Multilayers and Low-Dimensional Semiconductors Structures*, Ed. J. M. Chamberlin *et al.*, Plenum Press, New York, P. 211 (1990).
12. L. Esaki and R. Tsu, *Superlattice and negative differential conductivity in semiconductors*, IBM J. Res. Develop. **14**, 61 (1970).
13. R. Tsu and G. Dohler, *Hopping conduction in "superlattice"*, Phys. Rev. **B12**, 680 (1975).
14. A. Sibille, J. F. Palmier, C.Minot, and F. Mollot, *High field perpendicular conduction in GaAs/AlGaAs superlattices*, Appl. Phys. Lett. **54**, 165 (1989).
15. A. Sibille, J. F. Palmier, H. Wang, J. C. Esnault, and F. Mollot, *Negative differential perpendicular velocity in GaAs/AlGaAs superlattices*, Solid State Electronics **32**, 1461 (1989).

16. F Beltram, F. Capasso, D. L. Sivco, A. L.Hutchinson, S. G. Chu, and A. Y. Cho, *Scattering-Controlled Transmission Resonances ans Negative Differential Conductance by Field Induced Localization in Superlattices*, Phys. Rev. Lett. **64**, 3167 (1990).
17. R. Tsu and L. Esaki, *Stark quantization in superlattices*, Phys. Rev. **B43**, 5204 (1991).
18. A. Sibille, *Calculations of Zener inter-miniband tunneling rates in superlattices*, Solid State Electron. **32**, 1455.
19. J. Avron, L. Gunther, and J. Zak, *Energy uncertainty in "Stark ladders"*, Solid state comun **16,** 189 (1974).
20. E.E. Mendez,F. Agullo-Rueda, and J. M. Hong, *Stark Localization in GaAs-GaAlAs Superlattices under an Electric Field*, Phys. Rev. Lett. **60**, 2426 (1988).
21. P. Voisin, J. Bleuse, C. Bouches, S. Gaillard, C. Alibert, and A. Regreny, *Observation of the Wannier-Stark Quantization in a Semiconductor Supelattice*, Phys. Rev. Lett. **61**, 1639 (1988).
22. E. E. Mendez, F. Agullo-Rueda, and J. M. Hong,, *Temperature dependence of the electronic coherence of GaAs/GaAlAs superlattices*, Appl. Phys. Lett. **56**, 2545 (1990).
23. H. Schneider, H. T. Grahn, K. v. Klitzing, and K. Ploog, *Resonance-Induced Delocalization of Electrons in GaAs-AlAs Superlattices*, Phys. Rev. Lett. **65**, 2720 (1990).
24. A. Alexandrou, E. E. Mendez, and J. M. Hong, *Interplay between Landau and Stark quantization in GaAs/$Ga_{0.65}Al_{0.35}As$ superlattices*, Phys. Rev. **B44**, 1934 (1991).
25. J. Feldmann, K. Leo, J. Shah, D. A. B. Miller, J. E. Cunningham, T. Meier, G. von Plessen, A. Schulze, P. Thomas, and S. Schmitt-Rink, *Optical investigation of Bloch oscillations in a semiconductor superlattice*, Phys. Rev. **B46**, 7252 (1992).
26. C. Waschke, H. G. Roskos, R. Schwedler, K. Leo, H. Kurz, and K. Kohler, *Coherent Submillimeter-Wave Emission from Bloch Oscillations in a Semiconductor Superlattice*, Phy. Rev. Lett. **70**, 3319 (1993).
27. T. Dekorsky, P. Leisching, K. Kohler, and H. Kurz, *Electro-optic detection of Bloch oscillations*, Phys. Rev. **B50**, 8106 (1994).
28. T. Meier, G. von Plessen, P, Thomas, and S. W. Koch, *Coherent Electric-Field Effects in Semiconductors,* Phys. Rev. Lett. **73**, 902 (1994).
29. e.g. J. C. Maan, Ref. 2, P. 347.

30. T. Duffield, R. Bhat, M. Koza, F. DeRosa, D. M. Hwang, P. Grabbe, and S. J. Allen, Jr., *Electron Mass Tunneling along the Growth Direction of (Al, Ga)As/GaAs Semiconductor Superlattices*, Phys. Rev. Lett. **56**, 2724 (1986).

31. G. Belle, J. C. Maan, and G. Weimann, *Measurement of the miniband width in a superlattice with interband absorption in a magnetic field parallel to the layers,* Solid State Commun. **56**, 65 (1985).

32. T. Duffield, R. Bhat, M. Koza, F. DeRosa, K. M. Rush, and S. J. Allen, Jr., *Barrier-Bound Resonances in Semiconductor Superlattice in Strong Magnetic Fields*, Phys. Rev. Lett. **59**, 2693 (1987)

33. T. Yajima and Y. Taira, *Spatial Optical Parametric Coupling of Picosecond Light Pulses and Transverse Relaxation Effects in Resonant Media,* J. Phys. Soc. Japan **47**, 1620 (1979).

34. J. J. LePore, *An improved technique for selective etching of GaAs and* $Ga_{1-x}Al_xAs$, J. Appl. Phys. **51**, 6441 (1981).

35. D. Y. Oberly, J. Shah, T. C. Damen, C. W. Tu, T. Y. Chang, D. A. B. Miller, J. E. Henry, R. F. Kopf, N. Sauer, and A. E. DiGiovanni, *Direct measurement of resonant and nonresonant tunneling times in asymmetric coupled quantum wells*, Phys. Rev. **B40**, 3028 (1989).

36. M. G. W. Alexander, M. Nido, W. W. Ruhle, and K. Kohler, *Quantum Mechanical and Real Tunneling Transfer Times between GaAs/* $Al_{0.35}Ga_{0.65}As$ *Quantum Wells*, Phys. Rev. **B41**, 12295 (1990).

37. B. Deveaud, A. Chomette, F. Clerot, P. Auvray, A. Regreny, R. Ferreira, and G. Bastard, *Subpicosecond luminescence study of tunneling and relaxation in coupled quantum wells*, Phys. Rev. **B42**, 7021 (1990).

38. K. Leo, J. Shah, E. O. Gobel, T. C. Damen, S. Schmitt-Rink, W. Schafer, and K. Kohler, *Coherent Oscillations of a Wave Packet in a Semiconductor Double-Quantum-Well Structure*, Phys. Rev. Lett **66**, 201 (1991).

39. H. G. Roskos,, M. C. Nuss, J. Shah, K. Leo, D. A. B. Miller, A. M. Fox, S. Schmitt-Rink, and K. Kohler, *Coherent Submillimeter-Wave Emission from Charge Oscillations in a Double-Well Potential*, Phys. Rev. Lett. **68**, 2216 (1992).

40. S. A. Gurvitz, I. Bar-Joseph, and B. Deveaud, *Quantum tunneling and relaxation in asymmetric coupled wells*, Phys. Rev. **B43**, 14703 (1991).

41. K. Leo, J. Shah, J. P. Gordon, T. C. Damen, D. A. B. Miller, C. W. Tu, J. E. Cunningham, and J. E. Henry, *Hole Tunnelling in GaAs/AlGaAs Heterostructures: Coherent vs. Incoherent Resonant Tunneling,* Phys. Rev. **B42**, 7065 (1990).

42. I. Bar-Joseph and S. A. Gurvitz, *Time-dependent approach to resonant tunneling and inelastic scattering*, Phys. Rev. **B44**, 3332 (1991).

43. B. Deveaud, J. Shah, T. C. Damen, B. Lambert, and A. Regreny, *Bloch Transport of Electrons and Holes in Superlattice Minibands: Direct Measurement by Subpicosecond Luminescence Spectroscopy*, Phys. Rev. Lett. **58**, 2582 (1987).

44. A. Sibille, J. F. Palmier, H. Wang, and F. Mollot, *Observation of Esaki-Tsu Negative Differential Velocity in GaAs/AlGaAs Superlattices,* Phys. Rev. Lett. **64**, 52 (1990).

45. G. Livescu, D. A. B. Miller, T. Sizer, D. J. Burrows, J. E. Cunningham, A. C. Gossard, and J. H. English, *High-speed absorption recovery in quantum well diodes by diffusive electrical conduction*, Appl. Phys. Lett. **54**, 748 (1989).

46. G. Livescu, A. M. Fox, D. A. B. Miller, T. Sizer, W. H. Knox, A. C. Gossard, and J. H. English, *Resonantly Enhanced Electron Tunneling Rates in Quantum Wells*, Phys. Rev. Lett. **63**, 438(1989).

47. J. A. Cavailles, D. A. B. Miller, J. E. Cunningham, P. Li Kam Wa, and A. Miller, *Simultaneous measurements of electron and hole sweep-out from quantum wells and modeling of photo-induced screening dynamics*, IEEE J. Quantum Electron. **28**, 2486 (1992).

48. D. A. B. Miller, D. S. Chemla, T. C. Damen, A. C. Gossard, W. Wiegmann, T. H. Wood, and C. A. Burrus, *Electric field dependence of optical absorption near the band gap of quantum well structures*, Phys. Rev. **B32**, 1043 (1985).

49. C. Minot, H. Le Person, J. F. Palmier, and F. Mollot, *Time-of-flight measurements of negative differential velocity and electron heating in GaAs/AlGaAs superlattices,* Phys. Rev. **B47**, 10024 (1990).

50. e.g. Ref. 1 pp. 237-302, and Ref. 3 pp 261-299.

51. M. M. Dignam and J. E. Sipe, *Exciton Stark ladder in semoconductor superlattices*, Phys. Rev. **B43**, 4097 (1991).

52. U. Fano, *Effects of Configuration interaction on Intensities and Phase Shifts*, Phys. Rev. **124**, 1866 (1961).

53. H. Beutler, Z. Phys **93**, 177 (1935).

54. S. Glutsch, U. Siegner, M.-A. Mycek, and D. S. Chemla, *Fano resonances due to magnetoexciton and continuum states in bulk semiconductors*, Phys. Rev. **b50**, 17009 (1994).

55. D. S. Chemla, A. Maruani, and E. Batifol, *Evidence of the Autoionizing Character of Biexctons*, Phys. Rev. Lett. **42**, 1075 (1979).

56. D. Y. Oberly, G. Bohm, G. Weimann, and J. A. Brum, *Fano resonances in the excitation spectra of semiconductor quantum well*, Phys. Rev. **B49**, 5757 (1994).

57. U. Siegner, M.-A. Mycek, S. Glutsch, and D. S. Chemla, *Ultrafast Coherent Dynamics of Fano Resonances in Semiconductors,* , Phys. Rev. Lett. **74**, 470 (1995).

58. S. A. Gurvitz and M. S. Marinov, Two-exponential decay from a double-well potential, Phys. Rev. **A40**, 2166 (1989).

58. J. Feldmann, T. Meyer, G. von Plessen, M. Koch, E. O. Gobel, P. Thomas, G. Bacher, C. Hartmann, H. Schweizer, W. Schafer, and H. Nickel, *Coherent Dynamics of Excitonic Wave Packets*, Phys. Rev. Lett. **70**, 3027 (1993).

Publications Related to This Work

1. G. Cohen and I. Bar-Joseph, *Time of Flight Spectroscopy of Electron Transport in Superlattices: From Band Transport to Stark Localization.,* Phys. Rev. **B46,** 9857 (1992).

2. G. Cohen, S. A. Gurvitz, I. bar-Joseph, B. Deveaud, P. Bergman, and A. Regreny, *Electron Decay from Coupled Quantum wells to a continuum: Observation of Relaxation Induced Slow Down,* Phys. Rev **B47**, 16012 (1993).

3. G. Cohen, I. Bar-Joseph, and Hadas Shtrikman, *Stark Ladder and Temporal Oscillations in a Narrow Band Superlattice,* Phys. Rev. **B50**, (1994).

4. G. Cohen, Hadas Shtrikman and I. Bar-Joseph, *Optical spectroscopy of Fano interference in a GaAs/AlGaAs superlattice in a magnetic field,* submitted to the Physical Review.

Appendix A

Here are the details of the MBE grown samples used in our experiments:

composition	Al mole fraction	width (Å)	dopants	dopants concentration
GaAs		1000	p	1×10^{19}
AlGaAs	0.3	3000	p	2×10^{18}
AlGaAs	0.3	5000	p	2×10^{17}
AlGaAs	0.3	500		
periodic structure, 100 periods of:				
AlGaAs	0.3	30		
GaAs		30		
end of periodic structure				
AlGaAs	0.3	500		
AlGaAs	0.3	13000	n	2×10^{17}

Table 1: Structure of the superlattice used in the experiments described in chapter 5.

composition	Al mole fraction	width (Å)	dopants	dopants concentration	growth time (seconds)
GaAs		2000	Si	3×10^{18}	625
As		0			60
periodic structure, 60 periods of:					
AlAs	1	20	Si	3×10^{18}	24.69
As		0	Si	3×10^{18}	1
GaAs		60	Si	3×10^{18}	17.65
As		0	Si	3×10^{18}	1
end of periodic structure					
periodic structure, 10 periods of:					
GaAlAs	0.192	200			47.51
GaAs		80			23.5
GaAlAs	0.192	200			11.88
GaAs		80			23.5
AlGaAs	0.192	L_2			
GaAs		700			205
end of periodic structure					
GaAs		800	Si	3×10^{18}	250

Table 2: Structures of the three CQWs samples (chapter 4). L_2 has values of 10Å, 20 Å and 50Å.

composition	Al mole fraction	width (Å)	dopants	dopants concentration	growth time (seconds)
GaAs		1000	Si	2.5×10^{18}	460
periodic structure, 13 periods of:					
AlGaAs	0.35	200	Si	2.5×10^{18}	90
GaAs		6	i		3
As		0			13
end of periodic structure					
GaAs		500	Si	2.5×10^{18}	230
As		0			231
GaAs		900			830
AlGaAs	0.45	22			10
periodic structure, 40 periods of:					
GaAs		93			91
AlGaAs	0.45	22			10
end of periodic structure					
GaAs		700			646

Table 3: Structure of the narrow band superlattice used in the experiments described in chapter 6 and 7.

Certificate of Originality

This thesis describes my original work. The Time resolved PL measurements, presented in chapter 5, were performed in collaboration with a French group headed by B. Deveaud at CNET, France.